TECHNISCHE
UNIVERSITÄT
WIEN

Development of a multi microphone impedance tube for acoustic material characterization

Master Thesis

Felix Robert Huber, BSc

TECHNISCHE UNIVERSITÄT WIEN

Master Thesis

Development of a multi microphone impedance tube for acoustic material characterization

carried out for the purpose of obtaining
the degree of Diplom-Ingenieur (DI),

submitted at TU Wien
Faculty of Mechanical and Industrial Engineering
by

Felix Robert Huber, BSc
Mat.No.: 01631787

under the supervision of
Assistant Prof. Dipl.-Ing. Dr.techn. Florian Toth
Institute of Mechanics and Mechatronics, E325

Vienna, February 18, 2024 Signature

Affidavit

I declare in lieu of oath, that I wrote this thesis and carried out the associated research myself, using only the literature cited in this volume. If text passages from sources are used literally, they are marked as such.

I confirm that this work is original and has not been submitted for examination elsewhere, nor is it currently under consideration for a thesis elsewhere. I acknowledge that the submitted work will be checked electronically-technically using suitable and state-of-the-art means (plagiarism detection software). On the one hand, this ensures that the submitted work was prepared according to the high-quality standards within the applicable rules to ensure good scientific practice "Code of Conduct" at the TU Wien. On the other hand, a comparison with other student theses avoids violations of my personal copyright.

Vienna, February 18, 2024 Signature

Acknowledgements

I would like to express my heartfelt gratitude to my partner, the ever-patient and understanding J. K., for their unwavering support and spontaneity, responsible for half the daylight and nature I saw in the last months.

A special shoutout to my diverse circle of friends, each playing a unique role in keeping me sane and smiling during this whirlwind adventure. To N.H. always keeping an eye on the fridge and an open ear with loads of support, to A.P. the most gentle person I know, who are the greatest people, besides A.W. and M.G., I had the honor to share a flat with. To A.G., the most improved player (MIP) over the course of extensive study breaks filled with Deewan, many side projects and gourmet snacks, as well as N.K. their manager and mastermind behind any legendary events in the past.

Huge thanks to my family, comprised of the wise S.W., the kind M.H., and the ever-sunny L.H. (also known as my sister) with a special talent in entertainment and situational comedy. Their persistent encouragement, endless love, outstanding food and occasional tabletop game evenings have made even the toughest challenges feel like a walk in the park.

And of course, to my supervisor, F.T., whose guidance, patience and knack for turning my rambling ideas into coherent sentences have been nothing short of miraculous. Without all of you, this thesis would have been about as organized as a noise signal inside a tube with bad termination.

Contents

Abstract

For measurements inside the unidirectional wave field, used to characterize acoustic material properties, impedance tube measurements are widely used. However, due to expensive hardware and proprietary systems, they typically come with a substantial price tag. This thesis tries to improve accessibility to these kind of systems by utilizing consumer grade hardware considerably reducing the financial commitment.

To compensate the emerging error and achieve similar results the incorporation of multiple microphones is investigated. Therefore, the classical two- and four microphone formulations are extended by two different methods utilizing a least squares fit and a multiple pair approach with windowed averaging.

It is shown that for higher frequencies there is no substantial difference between professional and consumer grade hardware. The multi microphone approaches shine at lower frequencies and node positions reducing severe deviations of the individual pairs to notably closer values to the baseline measurement. This is not only evaluated visually, but also by utilizing a modified error measure, defined by power, to quantify the deviations in reflection- and transmission coefficients.

The many tests proved, that the accurate microphones and calibration is essential for good measurement results, but can be partially compensated by multi microphone algorithms. Additionally, several ideas to further improve the performance of the examined algorithms are posed pushing them closer to their full potential.

Kurzfassung

Das Impedanzrohr ist ein weit verbreitetes Instrument für die Bestimmung akustischer Materialparameter im unidirektionalen Schallfeld. Da für diese Messungen hochgenaue Hardware benötigt wird und diese nur von wenigen Herstellern angeboten wird, sind diese Messsysteme meist sehr teuer. Durch die Verwendung von herkömmlichen Bauteilen, soll in dieser Arbeit ein zugänglicheres Messystem entwickelt werden.

Um den damit einhergehenden Fehler zu kompensieren, werden zusätzliche Mikrofone verbaut. Folglich müssen auch die klassischen Algorithmen wie die Zwei- und die Vier-Mikrofon-Methode erweitert werden. In diesem Fall wird dazu die Methode der kleinsten Quadrate verwendet, aber auch ein Ansatz, bei dem die unterschiedlichen Mikrofonpaarungen über ihren validen Frequenzbereich gemittelt werden.

Es wurde gezeigt, dass die zusätzlichen Mikrofone bei hohen Frequenzen keinen signifikanten Unterschied machen. Bei niedrigen Frequenzen und Knotenpunkten der stehenden Wellen konnten die auftretenden starken Messfehler gut kompensiert werden. Die Ergebnisse wurden nicht nur graphisch mit den Referenzmessungen verglichen, sondern auch mit einem aus der Norm adaptierten Maß, dass den Leistungsfehler von Reflexions- und Transmissionskoeffizienten bestimmt.

Die vielen Versuche haben gezeigt, dass die Kleinsignalauflösung der Mikrofone essenziell für gute Messergebnisse ist. Fehler in diesem Bereich konnten aber teilweise gut von den zusätzlichen Mikrofonen abgefangen werden. Außerdem werden mehrere Verbesserungsvorschläge für das vorgestellte Messsystem aufgeworfen, um sie noch etwas näher an ihr volles Potential zu bringen.

List of Figures

List of Tables

Acronyms

1LM one-load method

2LM two-load method

2MIC two microphone

4MIC four microphone

ADC analog digital converter

API application programming interface

DAC digital analog converter

DFT discrete Fourier transform

FR frequency response

JSON JavaScript object notation

LRSM locally resonant sonic material

LSTSQ least squares

LT large tube

MISO multiple input single output

MPAIR multiple pair

PDE partial differential equation

SPL sound pressure level

ST small tube

Nomenclature

Notations

$\frac{\mathrm{d}\square}{\mathrm{d}t}$, $\frac{\partial\square}{\partial t}$	total and partial time derivatives of $\square$
$\mathcal{F}\{\square\}$	Fourier transform of quantity $\square$
$\square^*$	complex conjugate of $\square$
$\square_\mathrm{I}$, $\square_\mathrm{R}$	incident and reflected quantities of $\square$
$\square_\mathrm{ref}$	reference quantity of $\square$
$\square_\mathrm{u}$, $\square_\mathrm{d}$	up- and downstream quantities of $\square$
$\square_m$	quantity of m^th microphone
$\square_\mathrm{max}$	maximum of $\square$
$\square_\mathrm{min}$	minimum of $\square$
$\widetilde{\square}$	complex quantity of $\square$
$f(\square)$	function of continuous quantity $\square$
$f[\square]$	function of discrete quantity $\square$

Symbols

α	sound absorption coefficient
α_cross	reflection coefficient crossover error
α_e	reflected power error
$\boldsymbol{f}$	external forcing
$\boldsymbol{T}$	transmission matrix
$\boldsymbol{x}$	position
Δf	frequency step size
γ	adiabatic index
λ_plate	circular plate eigenmode
BT	bandwidth time product
TL	sound transmission loss
∇	Nabla operator
ω	angular frequency
Φ	phase angle
ρ	acoustic density of air
ρ_0	reference density of air
τ	sound transmission coefficient
τ_cross	transmission coefficient crossover error
τ_e	transmitted power error

ϑ	Celsius temperature
c_0	speed of sound
c_{FR}	frequency response calibration factor
c_{SPL}	sound pressure level calibration factor
D	tube diameter
f	continuous frequency
f_{l} , f_{u}	lower and upper frequency limits
f_{S}	sampling frequency
f_c	critical (resonance) frequency
$G_{\square,\square}$	auto- / cross-spectrum
h	relative humidity
$H_{\square,\square}$	transfer function
$j = \sqrt{-1}$	imaginary property
K	general constant
k	discrete frequency index
k_0	wave number
k_{l} , k_{u}	lower and upper discrete frequency limits
L	length
M	number of microphones
m_{sample}	mass of specimen
N	window length
n	discrete time index
p	acoustic sound pressure
p_0	atmospheric pressure
r	sound reflection coefficient
s	distance between microphones
T	absolute Kelvin temperature
t	continuous time
t_{rec}	recording time
t_{S}	sampling interval
u	signal
v	acoustic particle velocity
w	window function
x	position axis in tube direction (specimen surface $x = 0$)
Y	acoustic admittance
Z	acoustic impedance

Chapter 1

Introduction

Sound has always accompanied living beings and was of particular importance for human evolution. Therefore, acoustic sciences show a long history trying to make an impact on this matter [1]. Nowadays, controlled sound waves are not just important for art and culture, but pose many technical applications in medicine, structural mechanics, and geology to just name a few examples. A central part is the characterization of acoustic waves and their behavior in different media leading to the field of experimental acoustics. Because handling acoustic waves, in order to achieve a controlled and repeatable measurement environment, proved to be difficult, 1866 the Kundt's tube was developed and named after its inventor August Kundt. Originally intended to investigate wave propagation of sound, it can also be used to generate unidirectional waves below a specific frequency limit [2], acting as a kind of modal filter [3, 184ff]. Nowadays, this device is generally referred to as an "impedance tube", as it is used to measure the acoustic impedance of material samples.

Next to the reverbation room method, described by ISO 354, impedance tube measurement systems are widely used to characterize acoustic material behavior. Thus there are several companies offering their proprietary measurement systems. The two widely used methods either use two (ISO 10534-2 [4]) or four (ASTM E2611-19 [5]) microphones to measure different acoustic material parameters related to reflection, absorption, transmission, and impedance. This is done by dividing the unidirectional waves inside the tube into incident and reflected part, which is also called wave decomposition. These decomposed waves are the initial parameters to compute various acoustic material properties.

Because the commercial impedance tube systems utilize high end hardware, implicating high production costs, this thesis aims to achieve similar results by only using affordable components. To compensate the emerging error, caused by using low priced electronics, the integration of multiple microphones is investigated. These additional microphones are intended to be used to average the subsequent errors and furthermore extend the measurement capabilities to lower frequencies. This thesis poses two different methods to incorporate these extra signals formulated for a general microphone quantity M. The first method is a least squares fit to solve the wave decomposition problem, which becomes over-determined due to the added microphones. The latter explores the use of multiple microphone pairing to compute the acoustic material properties. The resulting quantities are then averaged after they are windowed according to their valid frequency range. To evaluate the performance of the posed methods an experimental setup, sketched in Fig. 1.1, is built. By utilizing of the shelf aluminum parts and 3D prints as structural components, as well as developing the power amplifier and microphones, costs are largely reduced. Commercial systems can cost up to a hundred thousand euros, while the developed system can be built below a thousand euros. Except for the baseline measurements, all results presented in this thesis were conducted with this system.

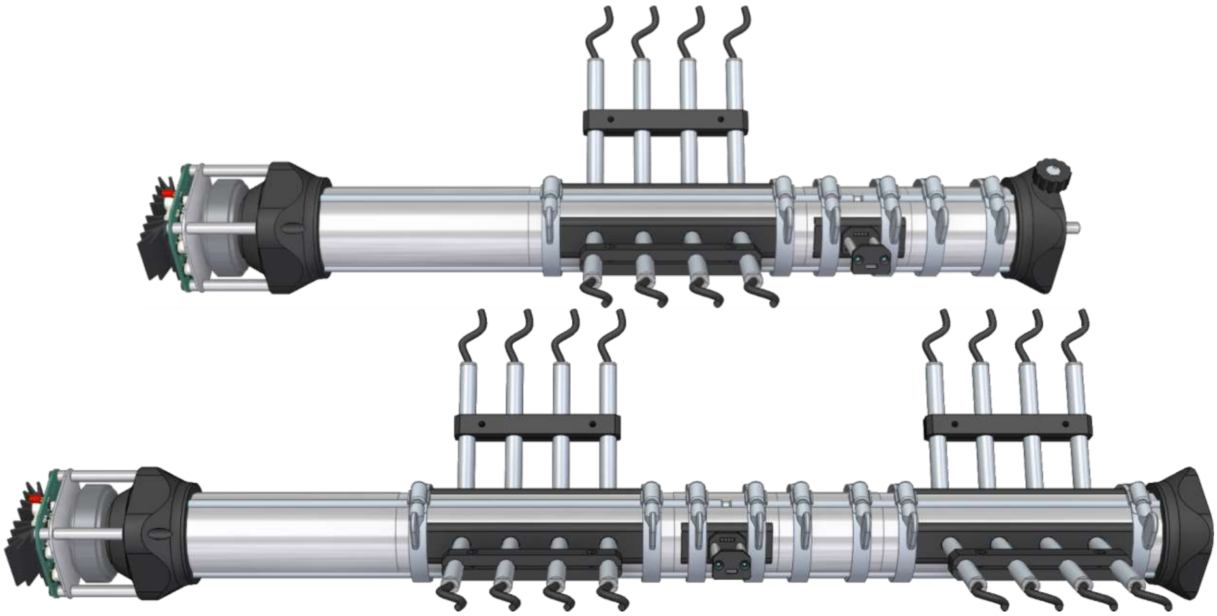

Figure 1.1: Experimental setups for reflection measurement ⓡ (top) and for transmission measurement ⓣ (bottom).

Outlining the thesis, initially relevant acoustic and signal processing fundamentals are covered. Continuing with recommended calibration routines, the two and four microphone method are introduced according to their respective standards, while including their valid frequency range. After that, averaging rules and the expected error sources are discussed, concluding Chapter 2. In Chapter 3 the developed hardware, electronics and software are explained. Additionally, the typical measurement procedure is outlined. After that, in Chapter 4, the baseline results are introduced alongside the definition of a scalar error measure to quantify the individual methods. The developed system is then used according to the standards to verify basic operation, reasoning found errors and deviations, before continuing to the advanced multi microphone methods posed by this thesis. The results of the different methods are compared and evaluated for accuracy and performance. Finally, Chapter 5 concludes the main findings and gives an outlook, raising possible improvements and further research ideas on this topic.

Chapter 2

Theory

To get a basic understanding of the procedures needed for impedance tube measurements this chapter summarizes the theoretical background needed to conduct this kind of acoustic experiments. Besides the involved physics, signal processing, as well as relevant standards for these topics are discussed, pursuing to provide relevant derivation, formulas, and resources to understand and reproduce acoustic material characterization inside an impedance tube. If the discussed standards differ in their selection of critical values and limits, the more restrictive parameters are used. This ensures compliance to all relevant standards.

2.1 Acoustic fundamentals

2.1.1 Basic acoustic equations

Newtons second law in continuum formulation yields the balance of momentum equation

$$\rho' \frac{\mathrm{d}\boldsymbol{v'}}{\mathrm{d}t} + \nabla p' = \boldsymbol{f}\,, \tag{2.1.1}$$

where ρ' denotes the density, $\boldsymbol{v'}$ the particle velocity vector and p' the pressure, balanced with the external forcing vector $\boldsymbol{f}$. Rewriting the total differential as partial differential for generalized 3D-coordinates yields

$$\rho' \frac{\partial \boldsymbol{v'}}{\partial t} + \nabla \frac{\boldsymbol{v'}^2}{2} - \boldsymbol{v'} \times (\nabla \times \boldsymbol{v'}) + \nabla p' = \boldsymbol{f}\,, \tag{2.1.2}$$

as the first basic acoustic partial differential equation (PDE). Secondly the mass balance equation is written in continuum formulation for a constant, but infinitesimal, control volume

$$\frac{\partial \rho'}{\partial t} + \nabla \cdot (\rho' \boldsymbol{v'}) = 0\,, \tag{2.1.3}$$

also known as the second basic acoustic PDE. Because state changes in acoustic waves happen really fast, there is not enough time for heat transfer. Therefore, one can assume ideal adiabatic state changes

$$\left(\frac{p'}{p_0}\right) = \left(\frac{\rho'}{\rho_0}\right)^{\gamma}\,, \tag{2.1.4}$$

with the adiabatic index γ. This is considered the third and final basic acoustic PDE.

With the assumption of small perturbation of a static basis, particle velocity $\boldsymbol{v'}$, pressure p' and density ρ' can be split up. Additionally, a negligibly small base velocity $\boldsymbol{v}_0$ is assumed, which means no base flow in the considered domain. The identities

$$\boldsymbol{v}' = \boldsymbol{v}_0 + \boldsymbol{v} \approx \boldsymbol{v} \tag{2.1.5}$$

$$p' = p_0 + p \tag{2.1.6}$$

$$\rho' = \rho_0 + \rho \tag{2.1.7}$$

can now be used to linearize the three basic acoustic equations in Eqs. (2.1.2) to (2.1.4). The quantities indexed with 0 are considered constant and in case of $\boldsymbol{v}_0$ also negligible small. Quantities with no index are the small perturbations, which are used for all further derivations.

Because of zero base flow $\boldsymbol{v}_0 = \boldsymbol{0}$, convective terms in Eq. (2.1.2) can be neglected. Assuming no external volume forcing yields

$$\rho_0 \frac{\partial \boldsymbol{v}}{\partial t} + \nabla p = 0\,. \tag{2.1.8}$$

Furthermore, the balance of mass in Eq. (2.1.3) simplifies to

$$\frac{\partial \rho}{\partial t} + \rho_0 \nabla \cdot \boldsymbol{v} = 0\,, \tag{2.1.9}$$

by splitting up the divergence term into constant and perturbed quantity. This equation is also referred as continuity equation. The ideal adiabatic gas Eq. (2.1.4) for perturbed quantities is additionally linearized using Taylor's expansion. Introducing the speed of sound c_0 further simplifies the equation to

$$p = c_0^2 \rho \quad \text{with} \quad c_0 = \sqrt{\gamma \frac{p_0}{\rho_0}}\,. \tag{2.1.10}$$

The equation set consisting of Eqs. (2.1.8) to (2.1.10) are the basic equations for acoustics problems [6, 11ff].

2.1.2 Linear homogeneous acoustic wave equation

By substituting Eq. (2.1.10) into Eq. (2.1.9), deriving this result with respect to time $\frac{\partial}{\partial t}$ and inserting Eq. (2.1.8) to remove the density, one obtains the linear homogeneous acoustic wave equation

$$\frac{1}{c_0^2} \frac{\partial^2 p(\boldsymbol{x}, t)}{\partial t^2} - \nabla \cdot \nabla p(\boldsymbol{x}, t) = 0\,, \tag{2.1.11}$$

where pressure is dependent on the position vector $\boldsymbol{x}$ and time t. This equation can be interchangeably formulated for density ρ and particle velocity $\boldsymbol{v}$ [6, 17ff].

2.1.3 Plane wave solution

As a general 1D-solution of the problem posed in Eq. (2.1.11) the propagating wave ansatz

$$p(x, t) = f_1(c_0 t - x) + f_2(c_0 t + x) \tag{2.1.12}$$

holds. Where the general functions f_1 and f_2 describe the shape of the waves propagating in positive and negative x-direction, respectively. For harmonic waves of angular frequency ω, traveling in positive x-direction, the general functions are replaced by a single cosine cos() with an additional phase shift Φ.

This yields

$$p(x,t) = p\cos(\omega t - k_0 x + \phi) \quad \text{with} \quad k_0 = \frac{\omega}{c_0}\,, \tag{2.1.13}$$

the harmonic ansatz with the wave number k_0 introduced for clearer writing [6, 22f]. For easier representation, one can use the complex amplitude $\widetilde{p}$ to combine amplitude and phase information into one complex number. The wave is now denoted in its complex representation

$$p(x,t) = \widetilde{p}e^{j(\omega t - k_0 x)}\,, \tag{2.1.14}$$

where Euler's formula $e^{jx} = \cos(x) + j\sin(x)$ is used to incorporate the phase shift [3, 476ff].

Substituting the harmonic ansatz from Eq. (2.1.13) into the 1D version of the mass balance in Eq. (2.1.9) yields

$$\rho_0 \frac{\partial v}{\partial x} = -\frac{1}{c_0^2}\frac{\partial\left(p\cos(\omega t - k_0 x + \phi)\right)}{\partial t}\,. \tag{2.1.15}$$

By evaluating both derivatives on the right side, as well as re-substituting the harmonic ansatz function, one can show the relation between pressure and particle velocity is constant, i.e.

$$\frac{p}{v} = \rho_0 c_0 \equiv Z_0\,, \tag{2.1.16}$$

defining the acoustic impedance Z_0, a specific constant for the propagation medium [6, p. 27]. It can be determined by the measurement methods proposed in this thesis.

2.2 Signal processing

For the measurement system presented in this thesis digital signal processing equipment is used. Therefore, some digital techniques have to be touched on. For many audio processing applications the acoustic pressure amplitude is needed in its complex discrete frequency representation $\widetilde{p}[k]$. To obtain this quantity from the analog microphone signal, the (simplified) processing chain

$$\widetilde{p}[k] = c_{SPL} \cdot \widetilde{c}_{FR}[k] \cdot \frac{2}{\sum_{n=0}^{N-1} w[n]} \sum_{n=0}^{N-1} (u[n] \cdot w[n]) e^{-j(2\pi/N)kn}\,, \quad k = 0, \ldots, N/2 \tag{2.2.1}$$

is used. The individual components of this chain are discussed below. The calibration factor c_{SPL} and c_{FR} are described in Section 3.2.

To represent a continuous signal in discrete time a constant sampling interval t_S is used to take "snapshots" of the signal u, i.e.

$$u[n] = u(nt_\mathrm{S}) \quad \text{with} \quad t_\mathrm{S} = \frac{1}{f_\mathrm{S}}\,, \tag{2.2.2}$$

used to express this process, where square brackets indicate a dependence on discrete time $[n]$ and round brackets on continuous time (t) [7, p. 12]. This sampling is conducted inside the USB soundcard with a set sampling frequency of $f_\mathrm{S} = 96\,\mathrm{kHz}$.

2.2.1 Discrete Fourier transform

To obtain the frequency representation of a signal the Fourier transform, a special case of the Laplace transform, is used. In discrete time the Laplace transform is replaced by the z-transform, from which the discrete Fourier transform (DFT) is derived over a finite duration of sequences N [7, p. 105]. The DFT $\mathcal{F}()$ as well as its inverse counterpart $\mathcal{F}^{-1}()$ are defined by

$$\begin{aligned} \widetilde{F}[k] &= \mathcal{F}(\widetilde{f}[n]) = \sum_{n=0}^{N-1} \widetilde{f}[n] e^{-j(2\pi/N)kn} , \quad k = 0, \dots, N-1 \quad \text{and} \\ \widetilde{f}[n] &= \mathcal{F}^{-1}(\widetilde{F}[k]) = \frac{1}{N} \sum_{n=0}^{N-1} \widetilde{F}[k] e^{j(2\pi/N)kn} , \quad n = 0, \dots, N-1 , \end{aligned} \tag{2.2.3}$$

where a capital $\widetilde{F}$ denotes the transformation of the time discrete function $\widetilde{f}$, with k as the discrete frequency [7, 651f]. Transformation into the frequency domain is conducted in software, utilizing a window length of $N = 8192$.

Because the sampled input signal is real valued, the DFT satisfies the conjugate symmetry property $\widetilde{F}[k] = \widetilde{F}^*[N-k]$. Therefore, only half of it has to be considered and the interval of k reduces to $k = 0, \dots, N/2$. For the software implementation, the corresponding functions `numpy.fft.rfft()` and `numpy.fft.irfft()` are used.

The frequency resolution can be computed by dividing the sampling frequency by the window length. For the chosen parameters one can write

$$\Delta f = \frac{f_\mathrm{S}}{N} = 11.72\,\mathrm{Hz} , \tag{2.2.4}$$

which poses a good compromise between frequency resolution and window size.

In order for the DFT defined in Eq. (2.2.3) to yield the same amplitudes as the time domain signal, the scaling term $1/N$ is moved from the inverse transformation to the forward transformation, resulting in the transformation provisions

$$\begin{aligned} \widetilde{u}[k] &= \frac{2}{N} \mathcal{F}(u[n]) , \quad k = 0, \dots, N/2 , \quad n = 0, \dots, N-1 \quad \text{and} \\ u[n] &= \frac{N}{2} \mathcal{F}^{-1}(\widetilde{u}[k]) , \quad n = 0, \dots, N-1 , \quad k = 0, \dots, N/2 . \end{aligned} \tag{2.2.5}$$

Due to the exploitation of symmetry, the DFT has to be additionally scaled by a factor of two consequently dividing the inverse by the same factor.

2.2.2 Windowing

To reduce spectral leakage a Hanning window $w[n]$ is multiplied with the input signal prior to the DFT as proposed in [5, 8.4.4]. Applying a window to the input signal invalidates the inverse DFT. However, this does not pose a problem as the inverse DFT is not needed for the impedance tube computations. For this thesis the Hanning window

$$w[n] = \begin{cases} 0.5 - 0.5\cos(2\pi n/N) & 0 \le n \le N , \\ 0 & \text{otherwise} , \end{cases} \tag{2.2.6}$$

is used [7, p. 560]. Note that windowing impacts the frequency resolution, smearing and broadening the Fourier transformed signal as discussed by Openheim [7, 832ff].

Because the window functions are typically normalized by their peak value, in order to maintain correct amplitudes the signal has to be divided by the mean value of the window. Derived from Eq. (2.2.5), the windowed and fully amplitude compensated DFT is written as

$$\widetilde{u}[k] = \frac{2}{N} \frac{N}{\sum_{n=0}^{N-1} w[n]} \mathcal{F}(u[n] \cdot w[n]) \,, \quad k = 0, \ldots, N/2 \,. \tag{2.2.7}$$

2.3 Calibration

The wave number k_0 is essential for accurate computations. For this thesis, no frequency dependence of the speed of sound c_0 and no attenuation [4, A.2.1.1] [5, 9.3.2] are assumed, resulting in a constant real valued wave number as function of frequency. Similarly one can formulate k_0 with respect to the discrete frequency k. Their relation is

$$k_0 = \frac{2\pi f}{c_0} = \frac{2\pi k f_\mathrm{S}}{c_0 N} \,. \tag{2.3.1}$$

The accuracy of k_0 still depends on a precisely known speed of sound. The methods proposed in ISO 10534-2 [4, 8.2] and ASTM E2611-19 [5, 8.2] express c_0 proportional to $\sqrt{T}$ and can be summarized as

$$c_0 = 343.2\,\mathrm{m\,s^{-1}} \sqrt{\frac{T}{293\,\mathrm{K}}} \,, \tag{2.3.2}$$

where T denotes the absolute temperature in Kelvin. Temperature should be measured prior to each measurement run, ensuring a precise wave number [4, A.1.2].

The characteristic acoustic impedance $Z_0 = \rho_0 c_0$ is affected by temperature and atmospheric pressure. For an accurate material parameter identification this characteristic impedance has to be precisely known. Additionally to the speed of sound, the density of air poses the other relevant component of the acoustic impedance. Both relevant standards express the density ρ_0 proportional to p_0/T [4, 8.2][5, 8.3] summarized by

$$\rho_0 = 1.186\,\mathrm{kg\,m^{-3}} \frac{293\,\mathrm{K}}{T} \frac{p_0}{101.325\,\mathrm{kPa}} \,, \tag{2.3.3}$$

with p_0 as atmospheric pressure. Therefore, additionally to the temperature, the atmospheric pressure needs to be measured regularly to ensure precise computations of the characteristic impedance and dependent quantities [4, A.1.3].

Before each measurement run, the microphones need to be calibrated. Absolute calibration is done in relation to a stable sound source e.g. a piston phone [4, A.1.1]. Each microphone has to be placed into this sound source to obtain the relation between measured quantity u_m and physical pressure value p_m in Pascal (Pa). Additionally, the frequency responses of the microphones have to be matched, to ensure precise measurement over the whole frequency range. Both standards introduce similar methods [4, 8.5] [5, 8.4.5.2] utilizing a microphone switching technique. First, a reference microphone, indexed "ref", has to be defined, followed by the measurements

$$\widetilde{H}^\mathrm{no}_{\mathrm{ref},m} = \frac{\widetilde{G}_{\mathrm{ref},m}}{\widetilde{G}_{\mathrm{ref,ref}}} = \frac{\widetilde{u}^*_\mathrm{ref}[k]\widetilde{u}_m[k]}{\widetilde{u}^*_\mathrm{ref}[k]\widetilde{u}_\mathrm{ref}[k]} \quad \text{and} \quad \widetilde{H}^\mathrm{sw}_{\mathrm{ref},m} = \frac{\widetilde{G}_{\mathrm{ref},m}}{\widetilde{G}_{\mathrm{ref,ref}}} = \frac{\widetilde{u}^*_\mathrm{ref}[k]\widetilde{u}_m[k]}{\widetilde{u}^*_\mathrm{ref}[k]\widetilde{u}_\mathrm{ref}[k]} \,, \tag{2.3.4}$$

where the latter is conducted with switched microphone positions. $\widetilde{G}_{i,i}$ and $\widetilde{G}_{i,j}$ denote the respective Auto- and cross-spectrum and the index ref, m indicates the microphone pair calibrated. Throughout this procedure the microphones need to be precisely placed to ensure high calibration quality. To correct the measured transfer function

$$\widetilde{H}_{\mathrm{ref},m} = \frac{\widetilde{H}^{\mathrm{measured}}_{\mathrm{ref},m}}{\widetilde{H}^{\mathrm{c}}_{\mathrm{ref},m}} \quad \text{with} \quad \widetilde{H}^{\mathrm{c}}_{\mathrm{ref},m} = \sqrt{\widetilde{H}^{\mathrm{no}}_{\mathrm{ref},m} \cdot \widetilde{H}^{\mathrm{sw}}_{\mathrm{ref},m}} \tag{2.3.5}$$

is used, where $\widetilde{H}^{\mathrm{c}}_{\mathrm{ref},m}$ denotes the calibration factor, $\widetilde{H}^{\mathrm{measured}}_{\mathrm{ref},m}$ the measured quantity, and $\widetilde{H}_{\mathrm{ref},m}$ the calibrated transfer function, to correct the frequency response of each measurement. This procedure enables accurate transfer functions over the whole frequency range.

2.4 Two microphone transfer function method

This method is documented in the ISO 10534-2 [4] standard and based on the frequency dependent sound pressure reflection factor $\widetilde{r}$. For this type of measurement, the impedance tube system utilizes two wall mounted microphones, indexed “A” and “B”, used to obtain their respective transfer function $\widetilde{H}_{\mathrm{A,B}}$. Furthermore, a solid piston ensures a reflective termination behind the specimen, which can be pulled back to set a “back volume” for advanced measurements. The setup is illustrated in Fig. 2.1, where the excitation is placed on the left end on the tube, while the specimen surface facing the excitation is defined as $x = 0$. To comply with the provisions in ISO 10534-2 [4, C], positive x-direction is pointing against the incident wave propagation direction. The tube diameter is denoted as D. Starting with $\widetilde{r}$ and the characteristic impedance Z_0, various acoustic material parameters can be derived. The equivalent American standard is the ASTM E1050-19 [8] not used in this thesis. To clear up the following derivation, frequency dependencies are not always indicated. Keep in mind that not only the complex pressure amplitudes $\widetilde{p}_m$, but also the wave number k_0 and resulting quantities are dependent on frequency.

For all the impedance tube techniques presented in this thesis, the first step is the wave decomposition inside the respective tube element. Thereby the sound pressure inside the tube is split into incident wave $\widetilde{p}_{\mathrm{I}}$ and reflected wave $\widetilde{p}_{\mathrm{R}}$ expressed by

$$\widetilde{p}_{\mathrm{I}}(x) = \widetilde{p}_{\mathrm{I}} e^{jk_0x} \quad \text{and} \quad \widetilde{p}_{\mathrm{R}}(x) = \widetilde{p}_{\mathrm{R}} e^{-jk_0x} \,. \tag{2.4.1}$$

These two wave components can then be used to assemble the pressures at the two microphone positions

$$\widetilde{p}(x_{\mathrm{A}}) = \widetilde{p}_{\mathrm{A}} = \widetilde{p}_{\mathrm{I}}(x_{\mathrm{A}}) + \widetilde{p}_{\mathrm{R}}(x_{\mathrm{A}}) = \widetilde{p}_{\mathrm{I}} e^{jk_0x_{\mathrm{A}}} + \widetilde{p}_{\mathrm{R}} e^{-jk_0x_{\mathrm{A}}} \quad \text{and} \tag{2.4.2}$$

$$\widetilde{p}(x_{\mathrm{B}}) = \widetilde{p}_{\mathrm{B}} = \widetilde{p}_{\mathrm{I}}(x_{\mathrm{B}}) + \widetilde{p}_{\mathrm{R}}(x_{\mathrm{B}}) = \widetilde{p}_{\mathrm{I}} e^{jk_0x_{\mathrm{B}}} + \widetilde{p}_{\mathrm{R}} e^{-jk_0x_{\mathrm{B}}} \,, \tag{2.4.3}$$

for the two microphones indexed “A” and “B” [4, C]. Solving the linear set of Eqs. (2.4.2) and (2.4.3) for the unknown pressure amplitudes $\widetilde{p}_{\mathrm{I}}$ and $\widetilde{p}_{\mathrm{R}}$ analytically yields

$$\widetilde{p}_{\mathrm{I}} = \frac{e^{jk_0(x_{\mathrm{A}}-x_{\mathrm{B}})} - \frac{\widetilde{p}_{\mathrm{B}}}{\widetilde{p}_{\mathrm{A}}}}{e^{jk_0(x_{\mathrm{A}}-x_{\mathrm{B}})} - e^{-jk_0(x_{\mathrm{A}}-x_{\mathrm{B}})}} \widetilde{p}_{\mathrm{A}} e^{-jk_0x_{\mathrm{A}}} = \frac{\widetilde{H}_{\mathrm{R}} - \widetilde{H}_{\mathrm{A,B}}}{\widetilde{H}_{\mathrm{R}} - \widetilde{H}_{\mathrm{I}}} \widetilde{p}_{\mathrm{A}} e^{-jk_0x_{\mathrm{A}}} \quad \text{and} \tag{2.4.4}$$

$$\widetilde{p}_{\mathrm{R}} = \frac{\frac{\widetilde{p}_{\mathrm{B}}}{\widetilde{p}_{\mathrm{A}}} - e^{-jk_0(x_{\mathrm{A}}-x_{\mathrm{B}})}}{e^{jk_0(x_{\mathrm{A}}-x_{\mathrm{B}})} - e^{-jk_0(x_{\mathrm{A}}-x_{\mathrm{B}})}} \widetilde{p}_{\mathrm{A}} e^{jk_0x_{\mathrm{A}}} = \frac{\widetilde{H}_{\mathrm{A,B}} - \widetilde{H}_{\mathrm{I}}}{\widetilde{H}_{\mathrm{R}} - \widetilde{H}_{\mathrm{I}}} \widetilde{p}_{\mathrm{A}} e^{jk_0x_{\mathrm{A}}} \,, \tag{2.4.5}$$

further simplified by the definition of the geometrical transfer functions

$$\widetilde{H}_{\mathrm{R}} = e^{jk_0(x_{\mathrm{A}}-x_{\mathrm{B}})} \quad \text{and} \quad \widetilde{H}_{\mathrm{I}} = e^{-jk_0(x_{\mathrm{A}}-x_{\mathrm{B}})} \,. \tag{2.4.6}$$

To form the transfer function $\widetilde{H}_{\mathrm{A,B}}$, instead of using the complex pressure amplitudes directly, one can

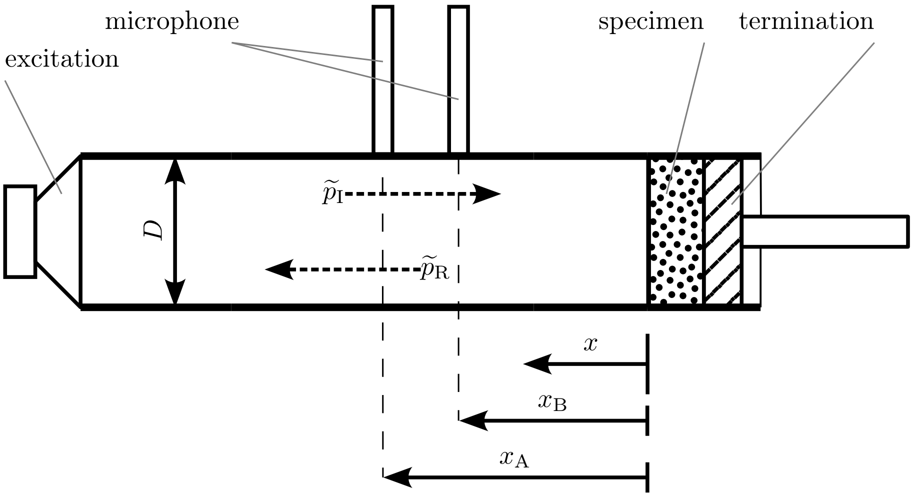

Figure 2.1: Two microphone (2MIC) method impedance tube setup.

utilize the cross- and auto-spectrum

$$\widetilde{H}_\mathrm{A,B} = \frac{\widetilde{H}_\mathrm{ref,B}}{\widetilde{H}_\mathrm{ref,A}} = \frac{\widetilde{G}_\mathrm{ref,B}}{\widetilde{G}_\mathrm{ref,A}}\,, \tag{2.4.7}$$

in order to improve averaging performance for deterministic signals as discussed in Section 2.7. This procedure is also part of ISO 10534-2 [4, 8.6] as well as ASTM E2611-19 [5, 8.5].

Inserting Eqs. (2.4.4) and (2.4.5) into the definition of the complex reflection coefficient $\widetilde{r}$ yields

$$\widetilde{r} = \frac{\widetilde{p}_\mathrm{R}}{\widetilde{p}_\mathrm{I}} = \frac{\widetilde{H}_\mathrm{A,B} - \widetilde{H}_\mathrm{I}}{\widetilde{H}_\mathrm{R} - \widetilde{H}_\mathrm{A,B}} e^{2jk_0x_\mathrm{A}}\,, \tag{2.4.8}$$

which can be used alongside the characteristic impedance Z_0 to compute the following, additional material parameters [4, 8.7f] [9]. The complex acoustic impedance $\widetilde{Z}$ is usually given in relation to the characteristic impedance Z_0 as

$$\frac{\widetilde{Z}}{Z_0} = \frac{1+\widetilde{r}}{1-\widetilde{r}}\,. \tag{2.4.9}$$

This is a very important material property widely used to define acoustic material behavior. One of many applications is the use in acoustic simulation [4, 8.9] [9]. The complex acoustic admittance $\widetilde{Y}$ is defined as the reciprocal of the acoustic impedance [4, 8.10], expressed by

$$\widetilde{Y} = \frac{1}{\widetilde{Z}}\,. \tag{2.4.10}$$

This property has its practical use for specific appliances, but is generally redundant because of its close relation to the acoustic impedance $\widetilde{Z}$. Lastly, the sound absorption coefficient α is a real valued quantity that can be computed as

$$\alpha = 1 - |\widetilde{r}|^2\,. \tag{2.4.11}$$

Defined as the fraction of incident power absorbed in the test specimen, the reflection coefficient is squared prior to subtraction [4, 8.8] [9]. Because it is real valued and easily understandable, this property is widely used in datasheets for acoustically absorbent materials [10][11].

2.5 Four microphone transfer function method

As of the time of writing, there is no ISO standard for transmission measurements inside an impedance tube. The only active standard covering this topic is the American standard ASTM E2611-19 [5]. The apparatus used for this type of measurement is sketched in Fig. 2.2. To distinguish acoustic quantities before and after the specimen $\square_\mathrm{u}$ is used for the upstream and $\square_\mathrm{d}$ for the downstream tube, respectively. The four microphones are placed in pairs on each side of the specimen, indexed "A" and "B" for the upstream- and "C" and "D" for the downstream pair. There are two different termination types anechoic (a) and blocked/open (b) to cover the open end of the downstream tube. Again the zero plane $x = 0$ is defined on the specimen surface facing the excitation, with the x-direction pointing against wave propagation direction. The tube diameter is denoted as D, while d denotes the specimen thickness. Due to the measurements inside both tube halves, quantities related to the transmission characteristics of the specimen can now be computed, again omitting the indication of frequency dependencies as discussed in Section 2.4.

The first step is the wave decomposition inside both tube sections separated by the mounted specimen. The pressure equations at the upstream microphone positions are therefore expanded by the downstream components, yielding the full set of equations

$$\widetilde{p}(x_\mathrm{A}) = \widetilde{p}_\mathrm{A} = \widetilde{p}_\mathrm{I,u}(x_\mathrm{A}) + \widetilde{p}_\mathrm{R,u}(x_\mathrm{A}) = \widetilde{p}_\mathrm{I,u} e^{jk_0 x_\mathrm{A}} + \widetilde{p}_\mathrm{R,u} e^{-jk_0 x_\mathrm{A}} \tag{2.5.1}$$

$$\widetilde{p}(x_\mathrm{B}) = \widetilde{p}_\mathrm{B} = \widetilde{p}_\mathrm{I,u}(x_\mathrm{B}) + \widetilde{p}_\mathrm{R,u}(x_\mathrm{B}) = \widetilde{p}_\mathrm{I,u} e^{jk_0 x_\mathrm{B}} + \widetilde{p}_\mathrm{R,u} e^{-jk_0 x_\mathrm{B}} \tag{2.5.2}$$

$$\widetilde{p}(x_\mathrm{C}) = \widetilde{p}_\mathrm{C} = \widetilde{p}_\mathrm{I,d}(x_\mathrm{C}) + \widetilde{p}_\mathrm{R,d}(x_\mathrm{C}) = \widetilde{p}_\mathrm{I,d} e^{jk_0 x_\mathrm{C}} + \widetilde{p}_\mathrm{R,d} e^{-jk_0 x_\mathrm{C}} \tag{2.5.3}$$

$$\widetilde{p}(x_\mathrm{D}) = \widetilde{p}_\mathrm{D} = \widetilde{p}_\mathrm{I,d}(x_\mathrm{D}) + \widetilde{p}_\mathrm{R,d}(x_\mathrm{D}) = \widetilde{p}_\mathrm{I,d} e^{jk_0 x_\mathrm{D}} + \widetilde{p}_\mathrm{R,d} e^{-jk_0 x_\mathrm{D}} \, . \tag{2.5.4}$$

Split into two linearly independent equation sets, one can use the upstream solutions from Eqs. (2.4.4) and (2.4.5) in combination with

$$\widetilde{p}_\mathrm{I,d} = \frac{e^{jk_0(x_\mathrm{C}-x_\mathrm{D})} - \frac{\widetilde{p}_\mathrm{D}}{\widetilde{p}_\mathrm{C}}}{e^{jk_0(x_\mathrm{C}-x_\mathrm{D})} - e^{-jk_0(x_\mathrm{C}-x_\mathrm{D})}} \widetilde{p}_\mathrm{C} e^{-jk_0 x_\mathrm{C}} = \frac{\widetilde{H}_\mathrm{R,d} - \widetilde{H}_\mathrm{C,D}}{\widetilde{H}_\mathrm{R,d} - \widetilde{H}_\mathrm{I,d}} \widetilde{p}_\mathrm{C} e^{-jk_0 x_\mathrm{C}} \quad \text{and} \tag{2.5.5}$$

$$\widetilde{p}_\mathrm{R,d} = \frac{\frac{\widetilde{p}_\mathrm{D}}{\widetilde{p}_\mathrm{C}} - e^{-jk_0(x_\mathrm{C}-x_\mathrm{D})}}{e^{jk_0(x_\mathrm{C}-x_\mathrm{D})} - e^{-jk_0(x_\mathrm{C}-x_\mathrm{D})}} \widetilde{p}_\mathrm{C} e^{jk_0 x_\mathrm{C}} = \frac{\widetilde{H}_\mathrm{C,D} - \widetilde{H}_\mathrm{I,d}}{\widetilde{H}_\mathrm{R,d} - \widetilde{H}_\mathrm{I,d}} \widetilde{p}_\mathrm{C} e^{jk_0 x_\mathrm{C}} \, , \tag{2.5.6}$$

the solutions for the downstream problem, to solve the full system.

According to ASTM E2611-19 [5, 3.1.2] the complex transmission coefficient $\widetilde{\tau}$ is defined as transmitted sound power divided by incident sound power. Therefore, additionally to incoming and outgoing pressures, the particle velocities have to be considered. These four relevant quantities are written as

$$\begin{aligned} \widetilde{p}(x=0) &= \widetilde{p}_0 = \widetilde{p}_\mathrm{I,u} + \widetilde{p}_\mathrm{R,u} & \widetilde{p}(x=d) &= \widetilde{p}_d = \widetilde{p}_\mathrm{I,d} e^{-jk_0 d} + \widetilde{p}_\mathrm{R,d} e^{jk_0 d} \\ \widetilde{v}(x=0) &= \widetilde{v}_0 = (\widetilde{p}_\mathrm{I,u} - \widetilde{p}_\mathrm{R,u}) \frac{1}{\rho_0 c_0} & \widetilde{v}(x=d) &= \widetilde{v}_d = \left(\widetilde{p}_\mathrm{I,d} e^{-jk_0 d} - \widetilde{p}_\mathrm{R,d} e^{jk_0 d}\right) \frac{1}{\rho_0 c_0} \, , \end{aligned} \tag{2.5.7}$$

where d denotes the sample thickness. The mentioned standard approaches this problem with a generalized transfer matrix formulation. From there, the coefficients of this matrix are used to compute the various material parameters. In general, this transfer matrix $\widetilde{\boldsymbol{T}}$ is introduced as

$$\begin{bmatrix} \widetilde{p}_\mathrm{a} & \widetilde{p}_\mathrm{b} \\ \widetilde{v}_\mathrm{a} & \widetilde{v}_\mathrm{b} \end{bmatrix}_{x=0} = \widetilde{\boldsymbol{T}} \begin{bmatrix} \widetilde{p}_\mathrm{a} & \widetilde{p}_\mathrm{b} \\ \widetilde{v}_\mathrm{a} & \widetilde{v}_\mathrm{b} \end{bmatrix}_{x=d} \, , \tag{2.5.8}$$

with the indices "a" for anechoic and "b" for blocked or open termination illustrated in Fig. 2.2. This test

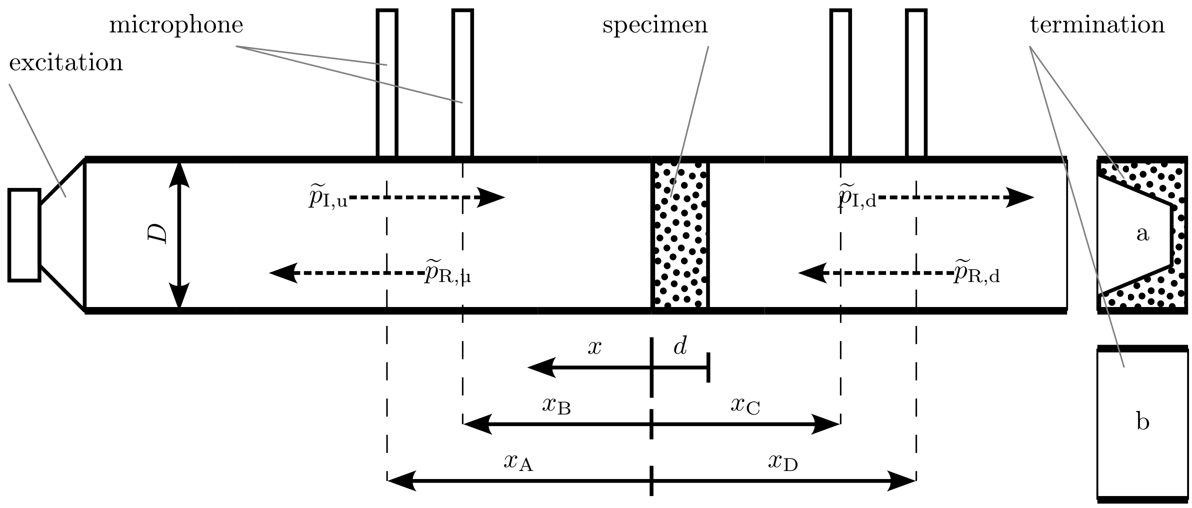

Figure 2.2: Four microphone (4MIC) method impedance tube setup.

is called the two-load method (2LM). Rearranging Eq. (2.5.8) to solve for the coefficients yields

$$\widetilde{\boldsymbol{T}} = \frac{1}{\widetilde{p}_{d,\mathrm{a}}\widetilde{v}_{d,\mathrm{b}} - \widetilde{p}_{d,\mathrm{b}}\widetilde{v}_{d,\mathrm{a}}} \begin{bmatrix} \widetilde{p}_{0,\mathrm{a}}\widetilde{v}_{d,\mathrm{b}} - \widetilde{p}_{0,\mathrm{b}}\widetilde{v}_{d,\mathrm{a}} & \widetilde{p}_{0,\mathrm{b}}\widetilde{p}_{d,\mathrm{a}} - \widetilde{p}_{0,\mathrm{a}}\widetilde{p}_{d,\mathrm{b}} \\ \widetilde{v}_{0,\mathrm{a}}\widetilde{v}_{d,\mathrm{b}} - \widetilde{v}_{0,\mathrm{b}}\widetilde{v}_{d,\mathrm{a}} & \widetilde{p}_{d,\mathrm{a}}\widetilde{v}_{0,\mathrm{b}} - \widetilde{p}_{d,\mathrm{b}}\widetilde{v}_{0,\mathrm{a}} \end{bmatrix} . \tag{2.5.9}$$

By assuming geometrical symmetric material properties, $\widetilde{\boldsymbol{T}}$ can be simplified with the identities $T_{11} = T_{22}$ and $T_{11}T_{22} - T_{12}T_{21} = 1$. Therefore, only one measurement with one termination is needed for computation (typically anechoic), naming this algorithm the one-load method (1LM) [5, 8.5.4]. The simplified transmission matrix can be expressed as

$$\widetilde{\boldsymbol{T}} = \frac{1}{\widetilde{p}_0\widetilde{v}_d - \widetilde{p}_d\widetilde{v}_0} \begin{bmatrix} \widetilde{p}_d\widetilde{v}_d - \widetilde{p}_0\widetilde{v}_0 & \widetilde{p}_0^2 - \widetilde{p}_d^2 \\ \widetilde{v}_0^2 - \widetilde{v}_d^2 & \widetilde{p}_d\widetilde{v}_d - \widetilde{p}_0\widetilde{v}_0 \end{bmatrix} . \tag{2.5.10}$$

Finally the transmission coefficient $\widetilde{\tau}$ can be computed by the four transmission matrix elements

$$\widetilde{\tau} = \frac{2e^{jkd}}{T_{11} + T_{12}/\rho_0 c_0 + \rho_0 c_0 T_{21} + T_{22}} . \tag{2.5.11}$$

Note that this definition of $\widetilde{\tau}$ applies for both transmission matrices, respectively the 1LM and the 2LM [5, 8.5.5.1] [12]. Exploitation of geometrical symmetry is discussed in Section 4.3.5, where measurement results of different methods are compared. The complex transmission loss $\widetilde{\mathrm{TL}}$ is the logarithmic reciprocal of $\widetilde{\tau}$, calculated with

$$\widetilde{\mathrm{TL}} = 10 \log_{10} \left(\frac{1}{\widetilde{\tau}} \right) . \tag{2.5.12}$$

This property is commonly used to define acoustic transmission characteristics of a material [5, 8.5.5.2] [12]. According to ASTM E2611-19 the first transmission matrix element can be used to describe the propagation wave number $\widetilde{k}'$ for the specimen material. The computational provision is formulated as

$$\widetilde{k}' = \frac{1}{d} \cos^{-1}\left(T_{11}\right) , \tag{2.5.13}$$

where $\cos^{-1}()$ denotes the complex inverse cosine [5, 8.5.5.5]. Additionally to the specific transmission characteristics, the transfer matrix method can be used to compute acoustic properties that are typical for the two microphone (2MIC) method [5, 8.5.5]. Starting with the most essential one, the complex reflection coefficient $\widetilde{r}$, computed by

$$\widetilde{r} = \frac{T_{11} - Z_0 T_{21}}{T_{11} + Z_0 T_{21}} , \tag{2.5.14}$$

which can be used to compute the various other material parameters introduced in Section 2.4.

By assuming small reflected waves $\widetilde{p}_{\mathrm{R,u}} \ll \widetilde{p}_{\mathrm{I,u}}$ and $\widetilde{p}_{\mathrm{R,d}} \ll \widetilde{p}_{\mathrm{I,d}}$ and again geometrical symmetry, one can derive a different formulation of the transmission coefficient proposed by Chung [9]. Applying the assumptions on Eqs. (2.5.7) and (2.5.10) yields

$$\boldsymbol{T} = \frac{1}{2\widetilde{p}_{\mathrm{I,u}}\widetilde{p}_{\mathrm{I,d}}e^{-jk_0 d}} \begin{bmatrix} \widetilde{p}_{\mathrm{I,d}}^2 e^{-2jk_0 d} + \widetilde{p}_{\mathrm{I,u}}^2 & \rho_0 c_0 (\widetilde{p}_{\mathrm{I,u}}^2 - \widetilde{p}_{\mathrm{I,d}}^2 e^{-2jk_0 d}) \\ (\widetilde{p}_{\mathrm{I,u}}^2 - \widetilde{p}_{\mathrm{I,d}}^2 e^{-2jk_0 d})/\rho_0 c_0 & \widetilde{p}_{\mathrm{I,d}}^2 e^{-2jk_0 d} + \widetilde{p}_{\mathrm{I,u}}^2 \end{bmatrix} . \tag{2.5.15}$$

Continuing by inserting into the definition of the transition loss Eq. (2.5.11) and simplifying the expressions yields the definition of transition loss by Chung

$$\widetilde{\tau} = \frac{\widetilde{p}_{\mathrm{I,d}}}{\widetilde{p}_{\mathrm{I,u}}} , \tag{2.5.16}$$

defined as the quotient of incident and transmitted pressure amplitudes. Because the taken assumptions depend on measurement setup and sample, results may vary a lot and the applicability has to be evaluated individually. For further discussion alongside measurement results on that topic Section 4.3.5 is recommended.

2.6 Working frequency range

Tube diameter, as well as the microphone spacing, effect the usable frequency range of the conducted measurement. Because of this it is crucial to define upper and lower frequency limit for each measurement appliance. The lower frequency limit only depends on the precision of measurement equipment used, but ISO 10534-2 [4, 5.2] recommends to set the microphone spacing to a minimum of 1.5 % of the wavelength. The upper frequency limit has two different dependencies. To additionally comply with ASTM E2611-19 [5, 6.5.4] the respective stricter limits are used yielding the joined formulations

$$f_{\mathrm{l}}(s) = 0.015\frac{c_0}{s} \quad \text{and} \quad f_{\mathrm{u}}(s) = \min\left(0.4\frac{c_0}{s}, 0.58\frac{c_0}{D}\right) , \tag{2.6.1}$$

where s stands for the "significant" microphone spacing. Which microphone spacing is "significant" depends on the limit itself and the algorithm used and is discussed in their respective sections. The same limits can also be formulated for the discrete frequency, written as

$$k_{\mathrm{l}}(s) = 0.015\frac{N}{f_{\mathrm{S}}}\frac{c_0}{s} \quad \text{and} \quad k_{\mathrm{u}}(s) = \frac{N}{f_{\mathrm{S}}} \min\left(0.4\frac{c_0}{s}, 0.58\frac{c_0}{D}\right) . \tag{2.6.2}$$

Because k is only defined on discrete intervals, the nearest value to the computet limits has to be used. To ensure computational efficiency, these limits are applied directly after the measurement signals are transformed into the frequency domain, truncating the pressure vectors computed with Eq. (2.2.1). Applying the systems frequency limits avoids divide by zero errors, as measurement data above or below the specified limits can be very unpredictable.

2.7 Averaging and error

This section deals with the various averaging concepts applied in the measurement process, in order to sustain consistent results and reduce the effects of various error sources. According to both relevant standards, for uniform materials a minimum of three samples should be tested. This reduces the effects of manufacturing inhomogeneities and defects. For non-uniform samples, the number should be even higher. For materials that are produced in bigger units, samples should be cut out at different positions in order to reduce the effect of local deviations[4, 7] [5, 7.4].

Because of the time delay, induced by the wave traveling from the microphone to the specimen and back, an error commonly known as time aliasing is introduced. This error is especially large for small window sizes combined with long distances. To minimize this effect, the measurement system should comply with the recommended minimum window size [4, D.2.2] [5, 9.3.1] in

$$\frac{2f_\mathrm{S}|x_\mathrm{max}|}{c_0} \approx 130 \ll N\,. \tag{2.7.1}$$

Due to the random white noise excitation signal, in theory, an infinite measurement time is needed to achieve a uniform frequency spectrum. For finite measurements the remaining error, also called random error, is reduced by averaging multiple time windows. To estimate how many of these DFT windows are needed, to keep this effect manageable, the product of frequency bandwidth B and recording time t_rec is considered. The recommended range is 50 to 100 [4, D.3] [5, 9.2]. The resulting BT product for a recording time of $t_\mathrm{rec} = 10\,\mathrm{s}$ and window length og $N = 8192$ can be cumputed as

$$\mathrm{BT} = \frac{f_\mathrm{S}}{N} t_\mathrm{rec} = 117.2 > 50 \ldots 100\,, \tag{2.7.2}$$

meeting the required criterion. As the result is part of the recommended interval, the averages can be considered accurate. Additionally, it is possible to compute the expected standard error

$$\sigma = \frac{1}{2\sqrt{\mathrm{BT}}} = 0.0462\,, \tag{2.7.3}$$

for a random noise excitation signal [4, D.3].

Instead of using the measured complex pressure amplitudes $\widetilde{p}_m$ directly, transfer functions in relation to a specified reference microphone are used [4, 8.6][5, 8.5.1f]. This allows the usage of cross- and auto-spectrum for efficient averaging. The standard definition of a transfer function, relative to a reference, is multiplied by the complex conjugate on both sides. The obtained spectra are then averaged individually, before they are used to form the transfer function. This process is described in

$$\widetilde{p_m} \longrightarrow \widetilde{H}_{\mathrm{ref},m} = \frac{\frac{1}{Q}\sum^Q G_{\mathrm{ref},m}}{\frac{1}{Q}\sum^Q G_{\mathrm{ref},m}} = \frac{\frac{1}{Q}\sum^Q \widetilde{p}^*_\mathrm{ref} p_m}{\frac{1}{Q}\sum^Q \widetilde{p}^*_\mathrm{ref}\widetilde{p}_\mathrm{ref}}\,, \tag{2.7.4}$$

with Q as the number of averages [13, 69ff]. For non overlapping windows, Q is closely related to BT and should follow the same criterion described in Eq. (2.7.2). By replacing pressures with their respective transfer functions the dimension is changed. As the primary results only consist of dimensionless coefficients, this change has no impact, because additional reference pressures are reduced in the computational process. Because of this, both relevant standards interchange pressures and transfer functions fluently with each other.

Amplitude and phase mismatches can cause large problems during the computation of the required transfer functions. By calibrating all microphones according to Section 2.3, these effects can be compensated, improving the overall quality and accuracy of the measurement [4, D.2.3f]. For long tubes acoustic waves are attenuated, influencing the measured pressure amplitudes and therefore the computational results. Because the distances between microphones and sample are short in respect to the used tube diameters, the attenuation is negligibly small for this application. This topic is also mentioned in Section 2.3, as it results in a real valued wave number k_0 [4, A.2.1.1] [5, 9.3.2].

Chapter 3

Developed methods

Subsequent to the state of the art, introduced in Chapter 2, the standardized methods are extended by introducing additional microphones. Starting of this chapter with the specifications of the impedance tube system that was built as part of this thesis. With the hardware specified, the algorithms to incorporate the additional measurement signals are presented, forming the centerpiece of this thesis. Finally, a brief overview of the software is given and the measurement procedure, used to conduct the experiments, is described.

3.1 Hardware

The measurement assemblies for both tube configurations are sketched in Fig. 3.1. The drawing is not to scale and the microphone positions are just for illustrative purposes. For clearer writing, the conventional methods microphones are hinted with the indices "A" and "B" for the up- and "C" and "D" for the downstream tube. For multi microphone measurements the general numeric index m is introduced, where $m = 1, \ldots, M_\mathrm{u}$ and $m = M_\mathrm{u} + 1, \ldots, M_\mathrm{u} + M_\mathrm{d}$ are used for the respective tube elements and the microphones are placed in the outlined modules. Each microphone module has two opposite 3D printed inlays, where microphones can be mounted. For the experiments conducted in this thesis, each module is equipped with eight microphones $M_\mathrm{u} = M_\mathrm{d} = 8$, arranged in four opposing pairs. Furthermore, the microphones are equally spaced with $s_\mathrm{min} = 35\,\mathrm{mm}$, yielding the resulting microphone x-positions, in relation to the specimen surface, listed in Table 3.1. Note that the corresponding array microphones used have to be defined for each individual measurement.

The excitation speaker is placed on one end of the impedance tube, coaxially radiating acoustic waves. To improve low frequency performance a broadband cone driver with a diameter of 80 mm is chosen. To attach it to the tube, a conical shaped adapter is used to merge the two different diameters. The zero point of the x-coordinate is set at the specimen surface. In accordance with ISO 10534-2 [4] the x-direction is defined as distance from the specimen surface, therefore pointing towards the excitation and against the propagation direction.

Table 3.1: Microphone x-positions in meters for up- and downstream tube by index m.

m	1	2	3	4	5	6	7	8	upstream
x_m	0.1225	0.1575	0.1925	0.2275	0.1225	0.1575	0.1925	0.2275	
m	9	10	11	12	13	14	15	16	downstream
x_m	-0.2275	-0.1925	-0.1575	-0.1225	-0.2275	-0.1925	-0.1575	-0.1225	

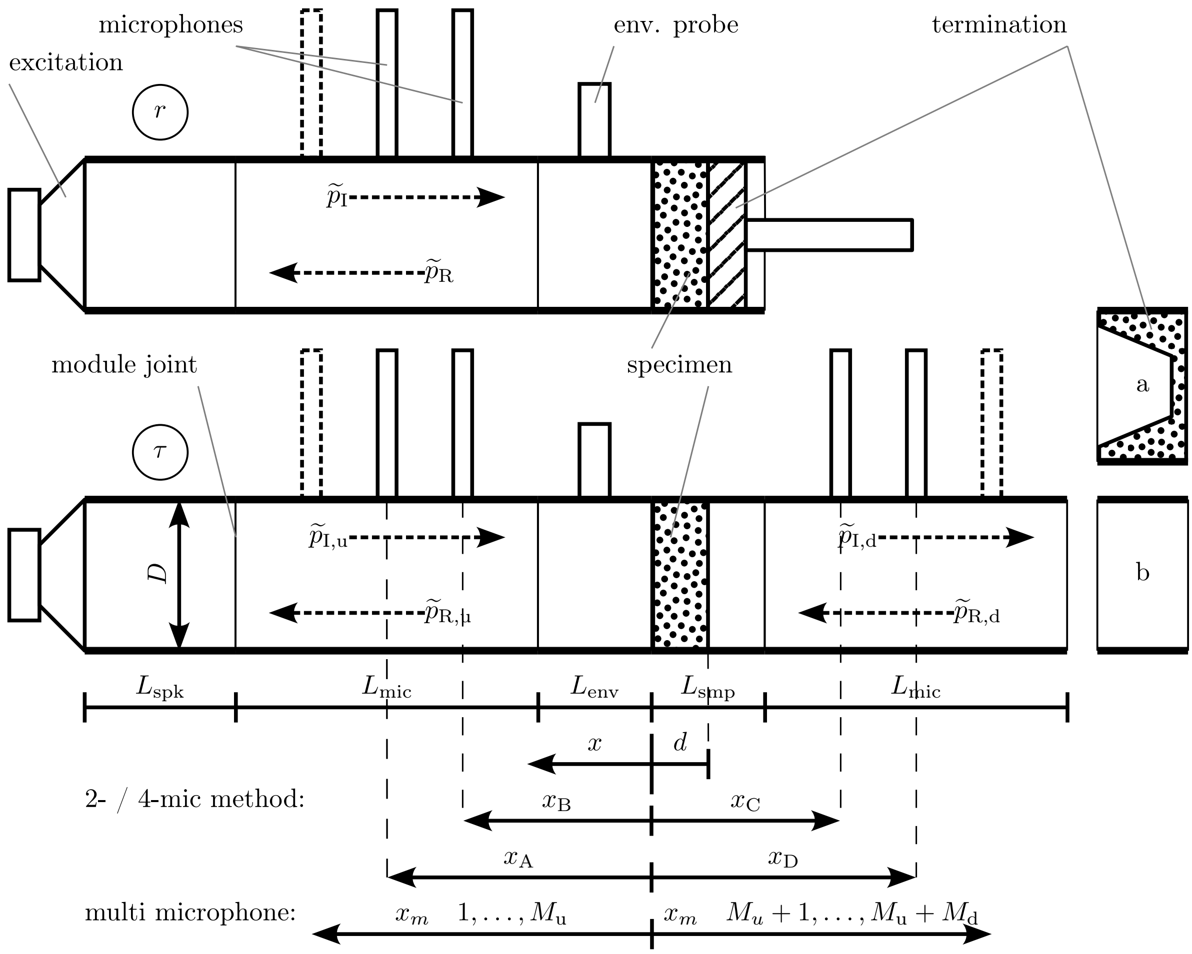

Figure 3.1: Hardware setup module arrangements, r for reflection coefficient, and τ for transmission coefficient measurements.

Setup r is used for reflection coefficient measurements. One microphone module with M_{u} microphones is placed between the excitation and specimen. The reflective termination is placed directly behind the specimen in form of a solid piston. This allows to set the termination according to the sample thickness, as well as setting a "back volume" for advanced measurements not covered in this thesis.

Setup τ can additionally measure transmitted waves and is therefore used for transmission coefficient measurements. Additionally to the two microphone modules used, this setup utilizes two different termination types, anechoic (a) and blocked/open (b), placed at the opposite side of the excitation. For the experiments conducted in this thesis an open tube is used for termination (b). To differentiate the two halves divided by the specimen, it is necessary to distinguish between upstream and downstream tube. The upstream tube lies between excitation and specimen, quantities referring to this tube are marked $\square_{\mathrm{u}}$. The downstream tube is defined between specimen and termination, related quantities are marked $\square_{\mathrm{d}}$. Note that the setup r only utilizes the upstream tube.

The environmental probe measures temperature, humidity, and static pressure inside the tube and is placed in a separate module in front of the sample. The importance of this sensor is discussed in Section 3.2. Dimensions are according to the limits of ISO 10534-2 [4] and ASTM E2611-19 [5] and are listed in Table 3.2. The sample thickness d is different for the individual specimen, see Section 4.1 for further details.

A good conversion from pressure to electric signal is substantial, to achieve accurate measurements. In contrast to the commercially used microphones, that can cost up to several thousand euros per capsule,

Table 3.2: Impedance tube dimensions in meters.

D	L_{spk}	L_{mic}	L_{env}	L_{smp}
0.050	0.150	0.200	0.075	0.075

the capsules used in this thesis are small electret capsules, widely available for about one euro per unit. To condition their signal and lower their output impedance, matching pre-amplifiers are designed according to the capsule specifications. The 3D model is displayed in Fig. 3.2. where 3D printing is used to support the printed circuit boards, while an aluminum tube acts as housing, shielding electromagnetic interference.

The microphones are connected to microphone amplifiers (RME Octamic II), which feature an additional gain stage, power delivery to the microphones, and integrated analog digital converters (ADCs). The signals are then digitally fed into the central audio interface (RME Fireface UFX+) connected to the host PC via USB. This audio interface features digital analog converters (DACs) used for excitation signal generation. Although the used converters are rather expensive, with a few thousand euros in total, cheaper hardware typically has similar specs and is more than suitable to conduct this type of measurements. Utilizing cheap microphone amplifiers (e.g. Behringer ADA8200) to extend a multi channel audio interface (e.g. Focusrite Scarlett 18i20) the total converter costs can be reduced way below a thousand euros.

The excitation signal is connected to a custom build power amplifier that mounts to the back of the cone speaker. Due to the physical combination of speaker and amplifier in the same module, versatility of the system is greatly improved. The environmental probe (Bosch BME280) mounts inside the tube and is connected via I2C-bus to a microcontroller (Raspberry Pi Pico) connected to the host PC via USB. To summarize, using the cheaper converters, a full multi microphone impedance tube system bellow a thousand euros is possible, while the commercial systems can cost up to a hundred thousand euros. Acoustic and environmental data is recorded and processed via a Python software introduced in Section 3.4.

3.2 Extended calibration

The tube mounted environmental probe is queried prior to each measurement enabling automatic temperature, humidity, and atmospheric pressure measurement. Additionally, the calibration routines suggested in Section 2.3 are extended for higher precision and for compatibility with the multiple microphone extensions. The wave number is dependent on the speed of sound, which was introduced indirectly proportional to $\sqrt{T}$. Since water vapor can alter the speed of sound, the method in Eq. (2.3.2) can be extended to also consider this phenomenon. Therefore, the polynomial approximation proposed by Wong

$$
\begin{aligned}
c_0 &= 331.29 \frac{c_h}{c_{\mathrm{ref}}} \sqrt{\frac{T}{273.15\,\mathrm{K}}} \mathrm{m\,s^{-1}} \quad \text{with} \\
\frac{c_h}{c_{\mathrm{ref}}} &= 1 + h \left(9.66\mathrm{e}{-4} + 7.22\mathrm{e}{-5}\vartheta + 1.8\mathrm{e}{-6}\vartheta^2 + 7.2\mathrm{e}{-8}\vartheta^3 + 6.5\mathrm{e}{-11}\vartheta^4\right)
\end{aligned}
\tag{3.2.1}
$$

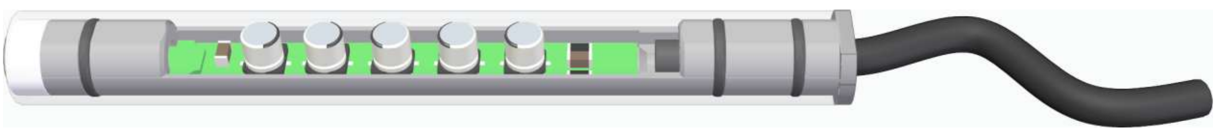

Figure 3.2: Custom developed microphone with electret capsule and internal pre-amplifier.

is used, introducing an additional scaling factor [14] [15], where ϑ denotes the Celsius temperature and h the relative humidity. Note that the polynomial coefficients are very small. With values $< 1\text{e}{-3}$ the humidity shows a minor effect compared to temperature and is therefore neglected in the standards. Wong estimates the maximum uncertainty of c_0 to be about 400 ppm.

To investigate the improvement in accuracy of the characteristic acoustic impedance, the method in Eq. (2.3.3) is extended to also consider the airs water content. To do this, the polynomial approximation presented by Wong [14] is used and additionally extended by the pressure scaling factor introduced in the standards [4, 8.2][5, 8.3]. Finally the characteristic acoustic impedance is expressed by

$$\begin{gathered} Z_0 = \rho_0 c_0 = 428.11 \frac{p_0}{101.325\text{kPa}} \frac{(\rho c)_h}{(\rho c)_{\text{ref}}} \sqrt{\frac{273.15\,\text{K}}{T}} \text{kg}\,\text{m}^{-2}\,\text{s}^{-1} \quad \text{with} \\ \frac{(\rho c)_h}{(\rho c)_{\text{ref}}} = 1 - h\left(1.3238\text{e}{-3} + 1.024\,04\text{e}{-4}\vartheta + 2.0624\text{e}{-6}\vartheta^2 + 1.11\text{e}{-7}\vartheta^3\right) \end{gathered} \tag{3.2.2}$$

introduced as humidity scaling factor. One can see that the consideration of humid air by polynomial extension is several magnitudes smaller than the effects of temperature, thus gains in accuracy are expected to be small.

The environmental quantities ϑ, T, h and p_0, are collected by the environmental probe inside the tube, which is queried prior to each measurement. For the experiments covered in this thesis a Bosch BME280 [16] sensor is used as it fulfills the requested accuracy of $T \pm 1\,\text{K}$, $h \pm 2\,\%$ and $p_0 \pm 0.5\,\text{kPa}$ [4, 5.11] [5, 6.7].

In accordance with Section 2.3, for the absolute calibration a sound calibrator with a sound pressure level (SPL) of 104 dB at a frequency of 1 kHz is used. After the microphone is placed inside the calibrator, the calibration factor c_{SPL} can be obtained by

$$c_{\text{SPL}} = \frac{p_{\text{ref}}}{|\widetilde{u}[k_{\text{SPL}}]|} \text{Pa} = p_{\text{ref}} \quad \text{with} \quad p_{\text{ref}} = 20\mu\text{Pa} \cdot 10^{\frac{104\,\text{dB}}{20\,\text{dB}}} \quad \text{and} \quad k_{\text{SPL}} = 1\,\text{kHz} \frac{N}{f_{\text{S}}}\,. \tag{3.2.3}$$

The frequency domain transformed measurement signal is denoted as $\widetilde{u}$. The discrete calibration frequency index k_{SPL} is used to select the transformed signal at the calibration frequency.

For the multi microphone techniques suggested in this thesis the switching technique, introduced in Section 2.3, is not practical. Therefore, a more basic approach inspired by ASTM E2611-19 [5, 8.4.5.3] is suggested. First, one has to define a reference microphone (ideally this microphone is calibrated by an external reference). Then the calibration factor $\widetilde{c}_{\text{FR}}$ in relation to the reference is calculated for each microphone m utilizing

$$\widetilde{c}_{\text{FR},m}[k] = \frac{\widetilde{c}'_{\text{FR},m}[k]}{\widetilde{c}'_{\text{FR},m}[k_{\text{SPL}}]} \quad \text{with} \quad \widetilde{c}'_{\text{FR},m}[k] = \frac{\widetilde{G}_{\text{ref,ref}}[k]}{\widetilde{G}_{\text{ref},m}[k]} = \frac{\widetilde{u}^*_{\text{ref}}[k]\widetilde{u}_{\text{ref}}[k]}{\widetilde{u}^*_{\text{ref}}[k]\widetilde{u}_m[k]}\,. \tag{3.2.4}$$

Auto- and cross-spectrum are expressed by $\widetilde{G}_{i,i}$ and $\widetilde{G}_{i,j}$, the index m indicates the respective microphone [13, 66ff]. Due to the absence of a perfect absorbing termination, an in place calibration was found impossible due to the wave patterns inside the tube. Therefore, this calibration requires the m^{th} microphone to be placed at the same x-position as the reference microphone, opposite inside the tube. The discrete SPL calibration frequency index k_{SPL} is used for normalization. Note that both introduced calibration factors are unique for each microphone.

3.3 Multiple microphone extension

The incorporation of additional microphones poses advantages, due to more measurements at different positions. This can improve measurement quality and frequency range by utilizing the effects of,

- individual microphone errors being compensated by averaging,
- always a microphones not at a node (low pressure point due to eigenmodes), improving transfer function quality,
- and different microphone spacing's allowing different frequency limits for evaluation.

Therefore, this thesis deals with the incorporation of additional microphones. In this section solutions for the multiple input single output (MISO) models

$$\widetilde{r} = \widetilde{r}\left(\widetilde{p}_1, \widetilde{p}_2, \ldots, \widetilde{p}_{M_\mathrm{u}}, x_1, x_2, \ldots, x_{M_\mathrm{u}}, k_0\right) \tag{3.3.1}$$

for setup (r) and

$$\widetilde{\tau} = \widetilde{\tau}\left(\widetilde{p}_1, \widetilde{p}_2, \ldots, \widetilde{p}_{M_\mathrm{u}+M_\mathrm{d}}, x_1, x_2, \ldots, x_{M_\mathrm{u}+M_\mathrm{d}}, k_0\right) \tag{3.3.2}$$

for setup (τ) are posed. The input vectors consist of the complex microphone pressures transformed into the frequency domain and their associated positions, yielding the reflection- or transmission coefficient. From there the other acoustic material properties can be derived as explained in Sections 2.4 and 2.5. M_u is the number of microphones in the upstream tube and M_d in the downstream tube. Note that the microphone index count starts at one and ends at $M_\mathrm{u} + M_\mathrm{d}$. This convention is arbitrary, but is used for consistency with the implementation.

To reduce the computational effort and improve averaging, instead of the pressure amplitudes, transfer functions to a known reference are used for the implementation. Section 2.7 explains this substitution and its benefits in more detail. However, for a clearer understanding and consistency in writing, the notation with pressure amplitudes is maintained.

3.3.1 Least squares fit

To combine the M microphone signals for each tube element, this approach uses a complex least square fit at the wave decomposition step. The generalized problem for upstream and downstream tube can be written as

$$\widetilde{p}(x_m) = \widetilde{p}_m = \widetilde{p}_{\mathrm{I,u}}(x_m) + \widetilde{p}_{\mathrm{R,u}}(x_m) = \widetilde{p}_{\mathrm{I,u}} e^{jk_0 x_m} + \widetilde{p}_{\mathrm{R,u}} e^{-jk_0 x_m} \quad 1, \ldots, M_\mathrm{u} \quad \text{and} \tag{3.3.3}$$

$$\widetilde{p}(x_m) = \widetilde{p}_m = \widetilde{p}_{\mathrm{I,d}}(x_m) + \widetilde{p}_{\mathrm{R,d}}(x_m) = \widetilde{p}_{\mathrm{I,d}} e^{jk_0 x_m} + \widetilde{p}_{\mathrm{R,d}} e^{-jk_0 x_m} \quad M_\mathrm{u}+1, \ldots, M_\mathrm{u} + M_\mathrm{d}\,. \tag{3.3.4}$$

For microphone counts of $M_\mathrm{u} > 2$ and $M_\mathrm{d} > 2$ the analytical solutions found in Sections 2.4 and 2.5 can not be applied, because the system of equations becomes over-determined. To solve the system one can rewrite it in matrix form and solve it as a linear least squares problem. For setup (r) only the upstream is of interest, posing the problem

$$\begin{bmatrix} e^{jk_0 x_1} & e^{-jk_0 x_1} \\ e^{jk_0 x_2} & e^{-jk_0 x_2} \\ \vdots & \vdots \\ e^{jk_0 x_{M_\mathrm{u}}} & e^{-jk_0 x_{M_\mathrm{u}}} \end{bmatrix} \begin{bmatrix} \widetilde{p}_{\mathrm{I,u}} \\ \widetilde{p}_{\mathrm{R,u}} \end{bmatrix} = \begin{bmatrix} \widetilde{p}_1 \\ \widetilde{p}_2 \\ \vdots \\ \widetilde{p}_{M_\mathrm{u}} \end{bmatrix}. \tag{3.3.5}$$

By inserting the solution for incident and reflected pressure amplitudes into Eq. (2.4.8), one obtains the complex reflection coefficient.

For setup Ⓣ, where upstream and downstream components are taken into account, both streams pose linearly independent problems. Therefore, Eq. (3.3.5) is still applicable and extended with the downstream formulation

$$\begin{bmatrix} e^{jk_0 x_{M_\mathrm{u}+1}} & e^{-jk_0 x_{M_\mathrm{u}+1}} \\ e^{jk_0 x_{M_\mathrm{u}+2}} & e^{-jk_0 x_{M_\mathrm{u}+2}} \\ \vdots & \vdots \\ e^{jk_0 x_{M_\mathrm{u}+M_\mathrm{d}}} & e^{-jk_0 x_{M_\mathrm{u}+M_\mathrm{d}}} \end{bmatrix} \begin{bmatrix} \widetilde{p}_{\mathrm{I,d}} \\ \widetilde{p}_{\mathrm{R,d}} \end{bmatrix} = \begin{bmatrix} \widetilde{p}_{M_\mathrm{u}+1} \\ \widetilde{p}_{M_\mathrm{u}+2} \\ \vdots \\ \widetilde{p}_{M_\mathrm{u}+M_\mathrm{d}} \end{bmatrix} . \tag{3.3.6}$$

The solution vector of the decomposed pressure amplitudes can again be used to compute the transmission coefficient, starting from Eq. (2.5.7). If the 2LM is required, the wave decompositions in Eqs. (3.3.5) and (3.3.6) have to be conducted for both termination types.

The valid frequency range is defined by using the maximum microphone spacing s_{max} for the lower and the minimum microphone spacing s_{min} for the upper frequency limit. Note that microphone spacing is determined for upstream or downstream tube separately. If they differ, the stricter limit has to be used. $f_\mathrm{l}(s_{\mathrm{max}})$ and $f_\mathrm{u}(s_{\mathrm{min}})$ can then be calculated utilizing Eq. (2.6.1).

3.3.2 Multiple pair measurement

For this method each unique microphone pair or quad is used to compute the required coefficient according to its respective standard. Depending on the spacing between the microphones used, the result is only valid on a certain frequency range. For setup Ⓡ, again, only the upstream tube is of interest, and the reflection coefficient is determined as described in Section 2.4. Upper and lower frequencies are computed for each pair, utilizing Eq. (2.6.2), to create a rectangular window function

$$w[k] = \begin{cases} 1 & k_\mathrm{l}(s_\mathrm{l})\frac{N}{f_\mathrm{S}} < k < k_\mathrm{u}(s_\mathrm{u})\frac{N}{f_\mathrm{S}} \, , \\ 0 & \text{otherwise} \, , \end{cases} \tag{3.3.7}$$

for simplicity. The use of other window functions is possible, but is not investigated in this thesis. To apply the pre-windowed average over unique microphone pairs the general calculation rule is written as

$$\square = \frac{\sum_{i=1}^{M} \sum_{j=i+1}^{M} \square_{ij} w_{ij}}{\sum_{i=1}^{M} \sum_{j=i+1}^{M} w_{ij}} \quad \text{for} \quad x_i \neq x_j \, , \tag{3.3.8}$$

where $\square$ is a placeholder for the quantity to average and the indices i and j indicate the dependency on the respective microphones. Note the index of the $\sum$-operators ensure unique microphone pairs, while summing over all M microphones. The additional rule $x_i \neq x_j$ prevents a pairing at the same x-position. This pre-windowed average algorithm can be extended to loop over unique quads, or rather pairs for up- and downstream tubes. It is formulated as

$$\square = \frac{\sum_{i=1}^{M_\mathrm{u}} \sum_{j=i+1}^{M_\mathrm{u}} \sum_{k=1}^{M_\mathrm{d}} \sum_{l=k+1}^{M_\mathrm{d}} \square_{ijkl} w_{ijkl}}{\sum_{i=1}^{M_\mathrm{u}} \sum_{j=i+1}^{M_\mathrm{u}} \sum_{k=1}^{M_\mathrm{d}} \sum_{l=k+1}^{M_\mathrm{d}} w_{ijkl}} \quad \text{for} \quad x_i \neq x_j \wedge x_k \neq x_l \, , \tag{3.3.9}$$

with an extended x-position criterion for up- and downstream pairs.

The pre-windowed average formulation introduced in Eq. (3.3.8) is utilized to average the complex reflection coefficient of each pair with

$$\widetilde{r} = \frac{\sum_{i=1}^{M_\mathrm{u}} \sum_{j=i+1}^{M_\mathrm{u}} \widetilde{r}(\widetilde{p}_i, \widetilde{p}_j, x_i, x_j) w(s)}{\sum_{i=1}^{M_\mathrm{u}} \sum_{j=i+1}^{M_\mathrm{u}} w(s)} \quad \text{for} \quad x_i \neq x_j \quad \text{and} \quad s = |x_i - x_j|\,. \tag{3.3.10}$$

The microphone spacing s is used to compute the frequency limits. For this part, it is just the absolute difference between both microphone coordinates applied for the lower and upper frequency limit.

For setup τ, a similar procedure is applied. Because microphone quads are used to conduct the four microphone (4MIC) method, spacing between upstream and downstream pairs can be different. This makes the constrains on the window function in Eq. (3.3.7) a bit more tricky. For the upper frequency limit the widest pair spacing s_u and for the lower frequency limit the lowest pair spacing s_l has to be used. These conditions are formulated in

$$s_\mathrm{l} = \min(|x_i - x_j|, |x_k - x_\mathrm{l}|) \quad \text{and} \quad s_\mathrm{u} = \max(|x_i - x_j|, |x_k - x_\mathrm{l}|)\,. \tag{3.3.11}$$

Again Eq. (2.6.2) can be applied to calculate the discrete frequency limits, which are then inserted into Eq. (3.3.7) to form the rectangular window. By applying the pre-windowed average for unique quads in Eq. (3.3.9) for the transmission coefficient, one can express the averaged solution as

$$\widetilde{\tau} = \frac{\sum_{i=1}^{M_\mathrm{u}} \sum_{j=i+1}^{M_\mathrm{u}} \sum_{k=1}^{M_\mathrm{d}} \sum_{l=k+1}^{M_\mathrm{d}} \widetilde{\tau}(\widetilde{p}_i, \widetilde{p}_j, \widetilde{p}_k, \widetilde{p}_l, x_i, x_j, x_k, x_l) w(s_\mathrm{l}, s_\mathrm{u})}{\sum_{i=1}^{M_\mathrm{u}} \sum_{j=i+1}^{M_\mathrm{u}} \sum_{k=1}^{M_\mathrm{d}} \sum_{l=k+1}^{M_\mathrm{d}} w(s_\mathrm{l}, s_\mathrm{u})}\,, \text{for } x_i \neq x_j \wedge x_k \neq x_\mathrm{l}\,. \tag{3.3.12}$$

Be ware that for the 2LM, recordings of both terminations have to be processed simultaneously.

These method complies closely to the provided standards, basically incorporating multiple measurements simultaneously into the same tube. ISO 10534-2 even proposes a similar method to combine results for different tube diameters, utilizing a linear crossover [4, 10]. If all possible pairs are used, the maximum and minimum frequencies for this method are defined by the minimum and maximum microphone distances respectively. See Section 3.3.1 for a detailed explanation.

3.4 Software implementation

Signal generation, recording, and processing is handled by a custom developed Python software. The connection to the audio interface is implemented by the PortAudio application programming interface (API), accessed by the `sounddevice` package. Calibration and setup data is loaded from JavaScript object notation (JSON) files. Signal generation and recording is handled in real-time using Python's builtin `threading` package.

During measurement the software streams the excitation signal to the DAC, while continuously recording all microphone signals from the ADCs. Theoretically, excitation and recordings can be latency compensated and therefore synchronized, but, because only transfer functions between microphones are used, this is not necessary.

The recordings are then processed according to the different methods introduced in this thesis. The input recordings are processed chunk by chunk, concurrently for all channels, by transforming each chunk in the frequency domain utilizing Eq. (2.2.1). Note that the calibration factors are applied during processing and are not baked into the recording, which allows calibration after the measurement. The transformed chunks are then averaged with the prescription in Eq. (2.7.4). The obtained transfer functions are now processed according to the selected method.

If further processing is conducted in Python, frequency and output quantity vectors are directly returned by the function handling the measurement. Alternatively, it is possible to store the results in a text file. Graphical evaluation, used to generate the figures in this thesis, is also implemented in Python. However, this is not integrated into the measurement software package yet.

3.5 Measurement procedure

Before each measurement series the tube should be fully calibrated. To start of the SPL calibration, each microphone is carefully removed from the tube and placed into the calibrator. After this is done the frequency response (FR) calibration is conducted inside the impedance tube utilizing reflective termination. By choosing a reference microphone all other microphones are calibrated to this reference. When the calibration candidate is placed opposite of the reference ($x_m = x_{\mathrm{ref}}$) and the random noise excitation signal is switched on, the calibration procedure is conducted. Note that unused microphone holes should be plugged to improve the quality of the wave field. After all candidates are calibrated, the calibration procedure is concluded.

In order to conduct a measurement, the impedance tube system is arranged in the respective setup. The sample carrier at $x = 0$ is detached and the specimen is pushed in until it sits flush with the separation plane. For reflective backed measurements, the piston is now pushed up to the other side of the specimen. After the sample holder is attached to the other tube elements, the whole assembly is placed on vibration damping pads. Now the measurement can be conducted by exciting a white noise signal and recording the microphones responses. During the measurement procedure all unused holes should be plugged, to keep the assembly airtight. Vaseline is used to seal the interfacing surfaces, as well as the perimeter of the mounted specimen. For transmission measurement with the 2LM, the terminations are exchanged between measurements. For open termination it is necessary to avoid objects at the outlet of the tube.

Although the environmental probe measures directly inside the tube, it is recommended to keep the environmental conditions stable throughout a measurement series, or additional calibration will be required. The excitation's SPL is manually adjusted to surpass the surrounding noise by at least 10 dB, in practice it became evident that this value is typically much higher.

Chapter 4

Results and Discussion

4.1 Samples and baseline

To benchmark the impedance tube used in this thesis, as well as the newly developed algorithms, it is essential to have a trusty baseline to compare to. Therefore, the materials are measured with a commercially available impedance tube system to determine their reflection and transmission coefficients. As described by both relevant standards and discussed in Section 2.7, three specimens of each material are used. The different samples are collected in Table 4.1. Some of them have an adhesive, covered by paper, on one side and are mounted with the adhesive surface facing away from the excitation.

The reference measurements are conducted at the Technical University of Graz utilizing Brüel & Kjær Type 4206 impedance and transmission loss measurement tubes. This system complies to the standards introduced in this thesis. To achieve a reference over a wide frequency range, the samples are measured with both tube diameters.he large tube (LT) with a diameter of 100 mm and a frequency range up to 1600 Hz and the small tube (ST) with a diameter of 29 mm and a frequency range from 500 Hz to 6400 Hz. Brüel & Kjær's PULSE material testing software is utilized to conduct calibration, measurement, and to compute the required quantities. After that, the results are combined for both tube diameters as suggested in ISO 10534-2 [4, 10i], discussed in detail for each quantity. In the following subsections the results of the reference measurements, as well as their plausibility are discussed.

Table 4.1: List of samples with reference name, properties, and thickness in meters.

Reference	Material	Supplier	Thickness d	Adhesive
B30	Basotect B	BASF	0.03	yes
B50	Basotect B	BASF	0.05	yes
G20	Basotect G+	BASF	0.02	yes
G30	Basotect G+	BASF	0.03	no
G50	Basotect G+	BASF	0.05	no

4.1.1 Baseline reflection coefficients

The setup used for the reflection coefficient measurements is similar to setup ⓡ. The results of LT and ST are combined utilizing the linear crossover

$$\widetilde{r}(f) = \begin{cases} \widetilde{r}_{\mathrm{LT}} & f \leq 500\,\mathrm{Hz}\,, \\ \widetilde{r}_{\mathrm{LT}} \frac{1600\,\mathrm{Hz}-f}{1100\,\mathrm{Hz}} + \widetilde{r}_{\mathrm{ST}} \left(1 - \frac{1600\,\mathrm{Hz}-f}{1100\,\mathrm{Hz}}\right) & 500\,\mathrm{Hz} < f < 1600\,\mathrm{Hz}\,, \\ \widetilde{r}_{\mathrm{ST}} & 1600\,\mathrm{Hz} \leq f\,, \end{cases} \tag{4.1.1}$$

where r_{LT} denotes the reflection coefficient measured in the large tube and r_{ST} the result in the small tube. Additionally, the difference in the overlapping domain is computed as

$$\alpha_{\mathrm{cross}} = ||\widetilde{r}_{\mathrm{LT}}|^2 - |\widetilde{r}_{\mathrm{ST}}|^2| \overset{!}{\leq} 0.05 \tag{4.1.2}$$

and averaged over the discrete frequency points. The reflection coefficient is additionally squared, because the criterion is formulated for the absorption coefficient, defined by acoustic power. ISO 10534-2 states, that this error should not be larger than 0.05 [4, 10i]. As described in Section 2.7, three specimens per material were used.

The results are plotted in Fig. 4.1 and the errors for the crossover region are listed in Table 4.2. Additionally, the minimum and maximum values for the three measured specimen are indicated by a translucent surface. Material B30 is not meeting the required criterion, while showing a small min-max deviation in the crossover region. Therefore, the error is not caused by differences between individual samples, but rather between the measurements of different tube diameters. One explanation are the different operators handling the impedance tube as suggested by Stender et al. [17]. Because of time restrictions during the reference measurements, operators switched several times. This hypothesis is further reinforced by the peak at 1600 Hz, which only shows for the ST diameter. This could be caused by a mounting error resulting in the reflective piston not touching the sample and allowing it to resonate, similar to the behavior seen for the transmission coefficient discussed in Section 4.3.4. However, there are no records that link operators and samples, making it impossible to verify this relation. Therefore, it is recommended to conduct additional reference measurements to dispose of this mismatch. Except for B30 all samples meet the required criterion and the results look plausible showing good overlap in the crossover region. The narrow band spikes at 2500 Hz are part of the baseline and are very likely a defect of the Brüel & Kjær system, because they stay at constant frequency for all samples. Applying third octave band averaging, as recommended in ISO 10534-2 [4, 10], would remove these narrow band peaks. Note that in the upper frequency region, the results show large variety for different material samples, indicated by the large min-max surface and spiking.

4.1.2 Baseline transmission coefficient

For transmission measurement, the Brüel & Kjær transmission loss measurement tubes are arranged similar to setup ⓣ. Again the same linear crossover, as expressed in Eq. (4.1.1), is applied to combine the results of LT and ST. Because the transmission coefficient is already a quotient of acoustic power,

Table 4.2: Crossover errors of baseline reflected power by sample.

	B30	B50	G20	G30	G50
α_{cross}	0.0822	0.0218	0.0252	0.0268	0.0304

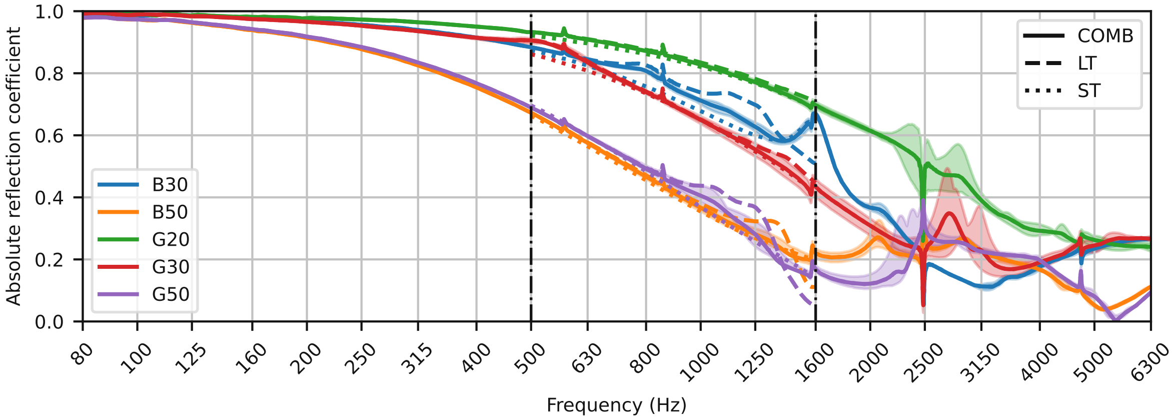

Figure 4.1: Baseline reflection coefficients obtained with small tube (ST), large tube (LT) and combined result (COMB) for different samples by color. Shaded regions indicate minimum and maximum of the three samples average.

the computation of crossover error can be written as

$$\tau_{\text{cross}} = ||\widetilde{\tau}_{\text{lt}}| - |\widetilde{\tau}_{\text{st}}|| \overset{!}{\leq} 0.05\,, \tag{4.1.3}$$

omitting the square compared to Eq. (4.1.2). This error is averaged over the crossover region and listed in Table 4.3.

Note that, compared to the reflection coefficient, the crossover region shows bad overlapping behavior. This is especially prominent in large crossover errors for samples with adhesives, which are measured with their protective paper film still on. Because of the imprecise baselines, samples with adhesive are not used for transmission measurement, leaving G30 and G50, whose results are plotted in Fig. 4.2. All measurements show a large dip in the low frequency region at 160 Hz, which can not be plausibly related to the expected physical behavior of the sample. Therefore, this dip is classified as system error. Additionally, there are strong deviations between LT and ST at the frequencies 500 Hz for G30 and 680 Hz for G50. These peaks are caused by sample resonance and are not part of the transmission coefficient. For more details see Section 4.3.4. All of this diminishes the plausibility of the results, adding to the discussion, when comparing the system developed for this thesis to the commercial impedance tube. For further details, all individual results can be found in Appendix A.

4.2 Average power error

To compare results of the different methods proposed by this thesis the average power error is introduced, which is inspired by the overlap criterion defined in ISO 10534-2 and already used in Sections 4.1.1 and 4.1.2. Furthermore, the limit of ±0.05, originally defined only on crossover sections [4, 10i], is used to classify the performance of the method under examination.

Because the error is compared by power, the square of the reflection coefficients is required. The error

Table 4.3: Crossover errors of baseline transmitted power by sample.

	B30	B50	G20	G30	G50
τ_{cross}	0.1239	0.1528	0.2622	0.0880	0.1038

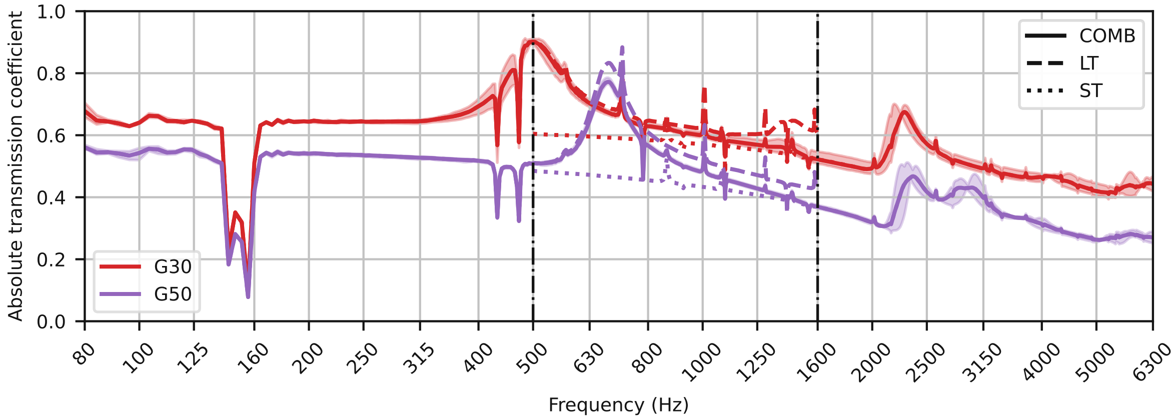

Figure 4.2: Baseline transmission coefficients obtained with small tube (ST), large tube (LT) and combined result (COMB) for different samples by color. Shaded regions indicate minimum and maximum of the three samples average.

can then be computed by

$$\alpha_\mathrm{e}[k] = |\widetilde{r}_\square[k]|^2 - |\widetilde{r}_\mathrm{base}[k]|^2 \,, \tag{4.2.1}$$

where the measurement results are marked by index. $\widetilde{r}_\mathrm{base}$ denotes the combined and averaged reflection coefficient of the baseline measurement and is compared to $\widetilde{r}_\square$, the averaged reflection coefficient measured in the experimental setup. Averaging $|\alpha_\mathrm{e}[k]|$ over the valid frequency range results in a scalar, which can be used to quantify the performance of the selected test method compared to the baseline. Averaging is done with

$$\alpha_{\mathrm{e},\square} = \frac{1}{k_u - k_l} \sum_{k=k_l}^{k_u} \left| |\widetilde{r}_\square[k]|^2 - |\widetilde{r}_\mathrm{base}[k]|^2 \right| \overset{!}{\leq} 0.05 \,, \tag{4.2.2}$$

where the final measure of error is indexed with the method compared to the baseline, utilizing $\square$ as a placeholder for the method under examination. The valid discrete frequency range can be computed with Eq. (2.6.2), considering the "significant" microphone spacing s of each method.

The same comparison quantity is now formulated for the acoustic transmission measurement. Because the transmission coefficient is already defined as a quotient of power, the error compared to the baseline can be directly computed by

$$\tau_\mathrm{e}[k] = |\widetilde{\tau}_\square[k]| - |\widetilde{\tau}_\mathrm{base}[k]| \,, \tag{4.2.3}$$

where the indices mark the affiliated measurements and $\square$ should be substituted for the used method. Averaging the identity $|\tau_\mathrm{e}[k]|$ over its valid frequency range yields

$$\tau_{\mathrm{e},\square} = \frac{1}{k_u - k_l} \sum_{k=k_l}^{k_u} \left| |\widetilde{\tau}_\square[k]| - |\widetilde{\tau}_\mathrm{base}[k]| \right| \overset{!}{\leq} 0.05 \,, \tag{4.2.4}$$

with the scalar measure for power error indexed again by $\square$. This averaging sum is very similar to the averaged reflected power error requiring the same discrete frequency limits denoted in Eq. (2.6.2).

4.3 Measurements according to standards

The results are obtained by the experimental setup described in Section 3.1 custom built for the experiments in this thesis. For clearer writing, results measured with this impedance tube are referenced by the method used to obtain the acoustic material parameters from the measurement data. This is possible, because this tube has only a single diameter of $D = 50\,\mathrm{mm}$. For comparisons to the baseline measurements LT, ST, or the index "base" for combined data are synonyms for quantities obtained by the commercial system. Results and discussion of these baseline measurements are fully covered in Section 4.1.

To classify the developed hardware, first, the standardized measurements are conducted and compared to the baseline acquired by the commercial Brüel & Kjær impedance tube system. On the basis of these comparisons one can evaluate the general performance of the system. This results are later used to quantify the accuracy of both multiple microphone methods. Additionally, this basic measurements shall be used to estimate, if errors are a result of the used hardware or originate from the method used. This is essential to pinpoint problems and poses a valuable contribution to the discussion.

4.3.1 Two microphone reflection coefficient

For this test the reflection coefficients are measured with the 2MIC method as described in Section 2.4. Therefore, the impedance tube is arranged in setup r. For this analysis the two microphone positions $x_\mathrm{A} = x_{m=2} = 0.1575\,\mathrm{m}$ and $x_\mathrm{B} = x_{m=1} = 0.1225\,\mathrm{m}$ are used, because they are closest to the specimen. Again three samples of each material are used. To allow a comparison between the baseline of the individual tube diameters and the obtained results, the combined baseline results are omitted for plotting. This gives the reader the opportunity to crosscheck, if one of the commercial tubes corresponds better or worse with the experimental setup. Additionally, the extreme values of the three used samples are indicated by a translucent surface around the averaged line plot. The average errors are calculated according to Eq. (4.2.2) and listed by material in Table 4.4.

A first look at the general trends of Fig. 4.3 shows, that the error increases drastically for frequencies below 630 Hz. Below 315 Hz the reflection coefficients even rise above one, meaning that the reflected wave has a larger amplitude than the incident wave. This is of course physically impossible and therefore has to be the result of some kind of error in the system. Above 630 Hz one can observe that the results and the baseline measurement track fairly well. For a full error over frequency plot refer to Appendix B. The materials B30 and G50 show deviation spikes in the frequency range between 1000 Hz and 1600 Hz. The errors originate partly in the measured results, which can be seen by comparing these spikes to the baseline. For B30 the errors emerge also in the baseline, where an additional mismatch between LT and ST is observed. Impedance tube measurements are very sensitive to mounting conditions posing a possible explanation for these offsets, as discussed in Section 4.1.1. Note that the averaged errors listed in Table 4.4 fully comply with the recommended interval.

As mentioned, the microphone positions were selected closest to the specimen. Theoretically the microphone selection should not make a difference, as long as the microphone spacing stays the same. For different microphone spacings the valid frequency range changes, but the results should be unaltered. By computing the average power error of each individual unique pair, one can quantify the error behavior, if a random pair would be chosen for the measurement. Additionally, the standard deviation is computed to express how wide the errors are scattered. The resulting errors of this investigation are listed in Table 4.4 and indicated by the "all" index.

The selected pair proves to be extremely good compared to the other possible pairs. The average power errors of the 2MIC method meet the criterion for all materials, and are even below the all-averages confidence interval, posing an outstanding choice. Figure 4.4 gives an overview of the impact of micro-

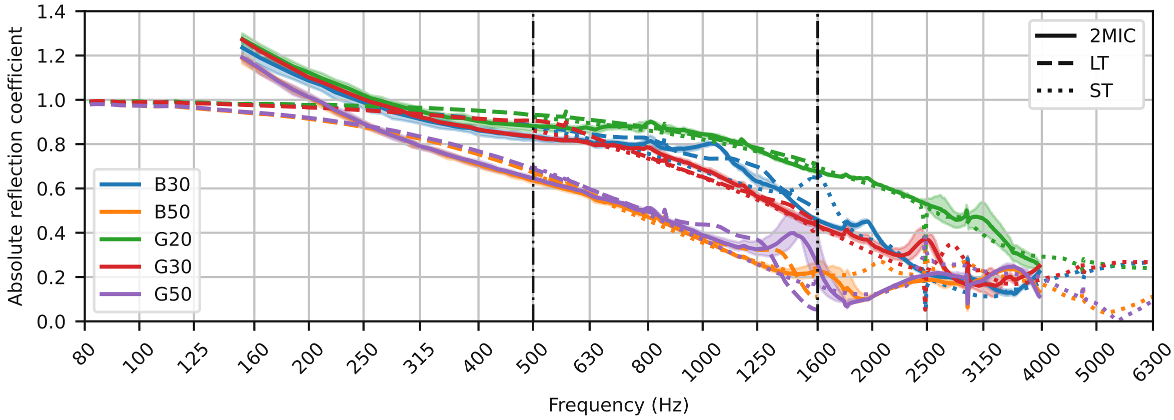

Figure 4.3: Reflection coefficients obtained with the two microphone (2MIC) method, compared to small tube (ST) and large tube (LT) baselines for different samples by color. Shaded regions indicate minimum and maximum of the three samples average.

Table 4.4: Averaged reflected power errors of two microphone (2MIC) method for the microphones closest to the specimen and all unique pairs averaged including standard deviations by sample.

	B30	B50	G20	G30	G50
$\alpha_{\mathrm{e,\ 2MIC}}$	0.0449	0.0257	0.0365	0.0417	0.0307
$\alpha_{\mathrm{e,\ all\text{-}2MIC}}$	0.0989 ± 0.0418	0.0626 ± 0.0299	0.1035 ± 0.0456	0.0865 ± 0.0380	0.0730 ± 0.0333

phone pair selection for material G50. Because of the equal microphone spacing discussed in Section 3.1, only three different microphone spacings are possible. These three spacings are grouped and marked with their respective line types. The lines represent the individual results, while the surfaces indicates the area in between. Large deviations can be clearly observed for lower frequencies, reaching way above physically possible limits (per definition, the reflection coefficient can not get larger than one). Looking deeper into the effects of the different pairs in Fig. 4.4, the pair deviations vanish at 400 Hz but come back maximizing at around 630 Hz. Plots for other materials are listed in Appendix C.

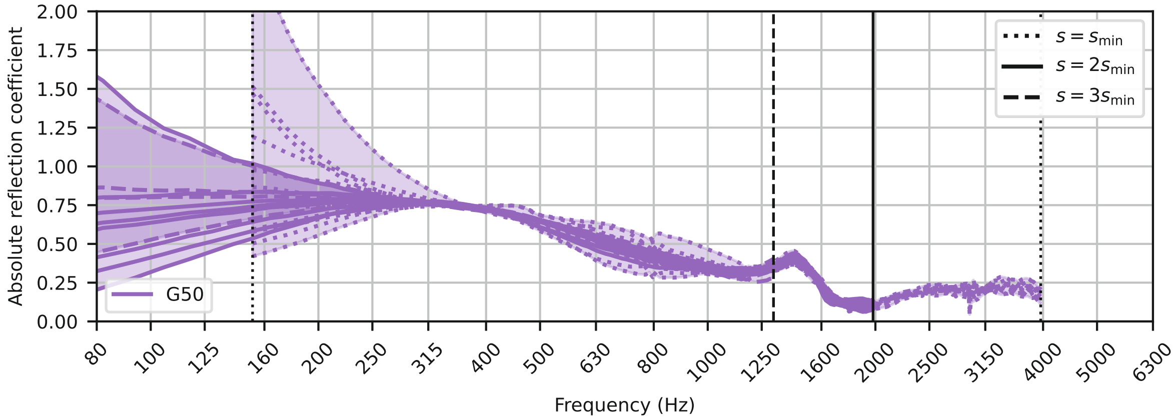

Figure 4.4: Reflection coefficients for G50, obtained with the two microphone (2MIC) method for different pairs selected and distinguished by microphone spacings s, resulting in different frequency limits indicated by the associated line styles. Shaded regions indicate minimum and maximum for each spacing.

4.3.2 Low frequency deviations

Considering the deviations returning at around 630 Hz, after a low spot at 400 Hz, and the increasing errors for low frequencies, one can pinpoint the problem to a bad measurement system performance at low signal differences, illustrated in Fig. 4.5. The introduced standards [4, 5.2] [5, 6.2.3] point out, that the lower frequency limit strongly depends on the accuracy of the measurement system. On one hand, the large wavelengths at low frequencies lead to small signal differences for closely spaced microphones. On the other hand, the first eigenfrequency of the tube results in low signals at the center where the microphones are placed. Approximating the speed of sound with $c_0 = 340\,\mathrm{m\,s^{-1}}$ one can estimate the first eigenfrequency for setup $\mathcal{T}$ at $f_1 = c_0/L = 680\,\mathrm{Hz}$. In contrast, measurements at $f_1/2 = 340\,\mathrm{Hz}$, where the amplitudes at the microphone module are maximized, result in the observed deviation minimum [18].

Probable causes are inaccuracies in the measurement hardware, where especially microphone capsules and their respective pre-amplifiers should be investigated. Additionally, the calibration factors deserve special consideration, because small errors in calibration can greatly influence the measurement error. These examinations are not covered by this thesis and are therefore recommended for further research.

4.3.3 Four microphone transmission coefficient

To compare the basic performance of transmission measurements, the experimental setup is arranged in configuration $\mathcal{T}$ and the corresponding microphone x-positions of $x_\mathrm{A} = x_{m=2} = 0.1575\,\mathrm{m}$, $x_\mathrm{B} = x_{m=1} = 0.1225\,\mathrm{m}$, $x_\mathrm{C} = x_{m=4+M_\mathrm{u}} = -0.1225\,\mathrm{m}$, and $x_\mathrm{D} = x_{m=3+M_\mathrm{u}} = -0.1575\,\mathrm{m}$ are selected, because they are nearest to the specimen. For this section the 2LM is used with the standard four microphone setup as described in Section 2.5. The averaged results over the three material samples are then compared to the measurements of two different commercial tube diameters. Applying Eq. (4.2.4) yields scalar error measures for each material, which are listed in Table 4.5. These quantities can then be used to evaluate the performance compared to the baseline.

Figure 4.6 displays the measurement results of the tested setup compared to the two baseline measurements. Again a strong rise in error for frequencies below 315 Hz, similar to the low frequency behavior of the reflection coefficient, is observed. Except for the low frequency drift, there are three main derivations from the center line marked by triangles. By looking at the comparison between results and baselines, one can see that the low frequency peaks are caused by the LT baseline measurement. For the mid frequency peaks the measurement setup is the main contributor, followed by the high frequency peaks induced by the ST baseline. All things considered, each tube exhibits a peak in transmission at a unique frequency, which will be addressed in Section 4.3.4. Outside of these three peaks and except for the discussed low frequency drift, the measurements correspond well with the baseline. The averaged errors are close to the set limit, but leave some room for improvement. The error over frequency plot can be found in

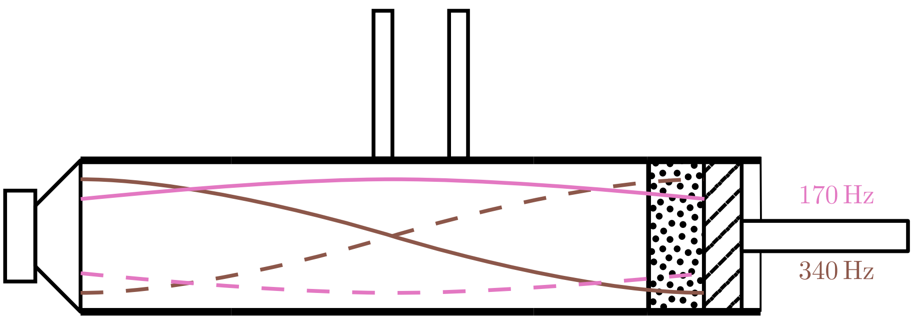

Figure 4.5: Pressure distributions for large wavelengths at low frequencies (pink) and eigenmodes (brown) resulting in small differences between microphones.

Appendix B.

Once more it is evaluated if the selected microphone quads, one pair closest from and after the specimen, perform especially well, or if any quad would result in a similar performance. Therefore, the averaged power error over all unique microphone quads or rather up- and downstream pairs is computed. The mean value as well as the standard deviation of the resulting errors are listed by material in Table 4.5, indicated by the “all” index.

It is evident, that the quad selected for basic measurements poses a really good choice by being clearly below the averaged error over all unique quads, even after subtracting the standard deviation. As visual overview the transmission coefficients of material G50 for a selection of individual quads are gathered into Fig. 4.7. Only quads with equal up- and downstream pair spacing are used to limit the possible frequency ranges. Compared to the reflection coefficients the deviations are smaller, but still pose physically impossible values for low frequencies, which can again be explained by the measurement systems inaccuracies for small differences. Note that for the transmission coefficients there is no clear frequency of minimum deviations. Because the tube for setup τ is much longer, the first eigenfrequency is low. Therefore, the node effect is outweighed by the small pressure differences due to large wavelengths.

4.3.4 Diameter unique peaks

Additionally to the bad low frequency behavior, discussed in Section 4.3.2, the measured transmission coefficients pose another type of deviation resulting in one peak unique for each tube diameter. These local peaks are marked with triangles throughout the plotted results and can be described by mechanical sample resonance.

First, the sample inside the tube is modeled by a basic mass-spring system coupled to the up- and downstream tube respectively. With the spring stiffness K_{spring} assumed constant over frequency for each material and by neglecting dampening and nonlinear effects, the resonance frequency is indirectly proportional to the square root of the total system mass [3, p. 163]. This relation is used to find the correlation between peak frequencies and tube diameters. For constant density of the material, and a circular sample of constant thickness, mass is proportional to the diameter squared, yielding the resonance frequency

$$f_{\text{c}} = \frac{1}{2\pi}\sqrt{\frac{K_{\text{spring}}}{m_{\text{sample}}}} \propto \frac{K_1}{D}\,, \tag{4.3.1}$$

where all constants are collected in K_1. Alternatively, the sample is modeled as a clamped plate. For undamped thin isotropic plates the equation of motion has analytical solutions, which show indirectly proportional behavior to the squared diameter written as

$$f_{\text{c}} = \frac{1}{2\pi}\frac{4\lambda^2_{\text{plate}}}{D^2}\sqrt{\frac{K_{\text{plate}}}{\rho d}} \propto \frac{K_2}{D^2}\,, \tag{4.3.2}$$

Table 4.5: Averaged transmitted power errors of four microphone (4MIC) method for the microphones closest to the specimen and all unique quads averaged including standard deviations by sample.

	G30	G50
$\tau_{\text{e, 4MIC}}$	0.0630	0.0776
$\tau_{\text{e, all-4MIC}}$	0.1193 ± 0.0294	0.0978 ± 0.0205

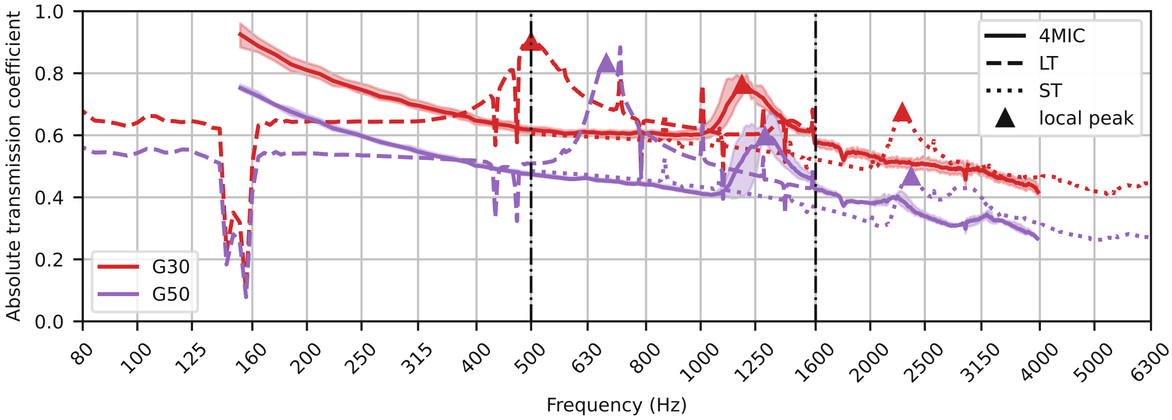

Figure 4.6: Transmission coefficients for G50, obtained with the four microphone (4MIC) method, compared to small tube (ST) and large tube (LT) baselines for different samples by color. Shaded regions indicate minimum and maximum of the three samples average and triangles mark significant deviations (local peaks).

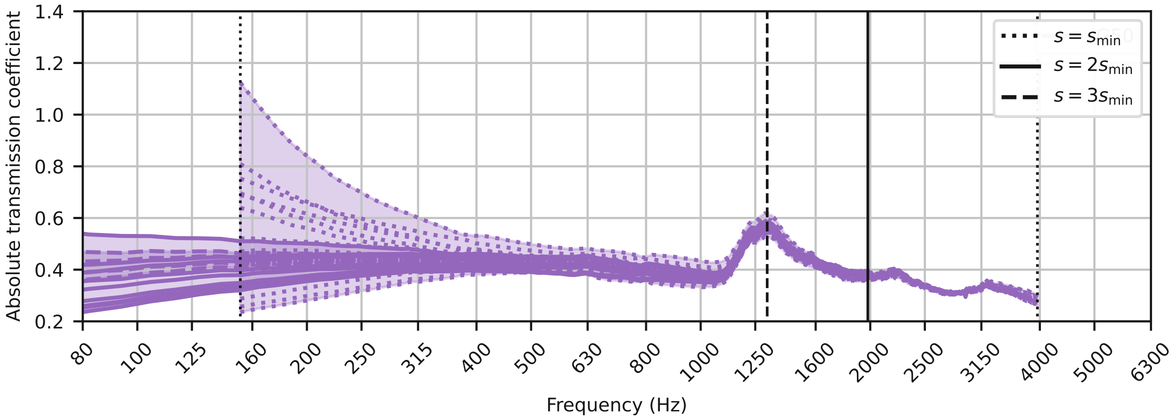

Figure 4.7: Transmission coefficients obtained with the four microphone (4MIC) method for different quads selected and distinguished by microphone spacings s, resulting in different frequency limits indicated by the associated line styles. Shaded regions indicate minimum and maximum for each spacing.

where λ_{plate} denotes the eigenmode, K_{plate} the bending stiffness and ρ the mass density. All newly introduced quantities are not dependent on the diameter and therefore collected in K_2 [19]. The peak frequencies from Fig. 4.6 are extracted and plotted as triangles in Fig. 4.8. Additionally, two least squares fits were used to adapt the proportionalities found in Eqs. (4.3.1) and (4.3.2) to the selected peak points.

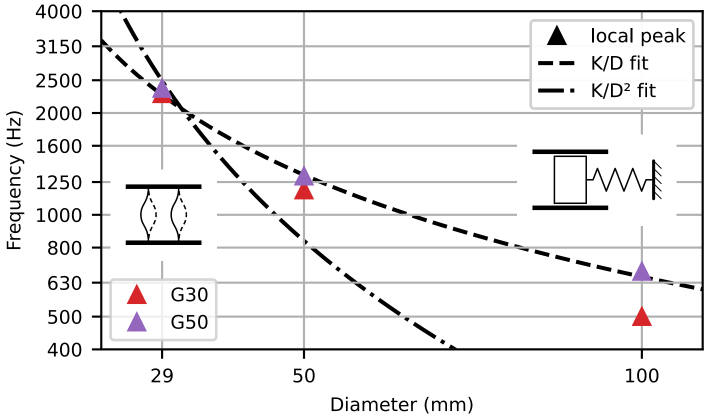

Figure 4.8: Resonance frequencies (local peaks) of each specimen (colors) by tube diameter, compared to a mass-spring system (K/D fit) and a plate bending model (K/D^2 fit).

Although both models are strongly simplified, compared to the real physical procedures inside the impedance tube and the porous specimen, one can see that the peaks fit in between the proposed proportional trends, where G50 mainly complies with the mass-spring system and G30 shows a slight shift towards plate-bending for a higher D/d ratio. Similar effects were observed by Ho et al., investigating locally resonant sonic materials (LRSMs) inside an impedance tube system [20]. Consequently the marked local peaks can be interpreted as results of the different tube diameters. Looking at the phase plot in Fig. 4.9 further reinforces this theory, where the phases experience a jump at the respective resonance frequencies, while the measurements conducted in other tube diameters stay constant.

4.3.5 Influence of reflected waves

To test the different computation methods of the transmission coefficient derived in Section 2.5, the results from the 1LM and the alternative definition by Chung [9] are compared to the 2LM. Instead of the baseline, the 2LM is used as reference to avoid confusion due to the different resonance peaks, and because it is considered the most accurate of the proposed 4MIC methods [5, 8.5.4]. Because both methods under investigation only use a single measurement, one can compute them for anechoic (a) and open (b) termination and compare their performance. The average transmission errors relative to the 2LM are displayed in Fig. 4.10 for material G50. Results for G30 look similar and are attached in Appendix D for completeness. The different methods are indicated by different line styles, terminations are marked by transparency.

For the lower frequency range, measurements with termination (b) exhibit large deviations, while termination (a) keeps the error low. For middle and upper frequencies Chung performs worse for both termination types. As described in Section 2.5, this method omits the reflected part in the wave decomposition. Therefore, better performance for anechoic termination is expected and clearly visible in the comparison. The 1LM performs better for both termination types, presenting smaller derivations over all frequency bands. This indicates that the selected samples display equal acoustic properties on both sides, also called geometrical symmetric [5, 8.5.4.2].

In general, the 2LM should be used whenever possible. If only one measurement can be conducted, the 1LM shows a similar performance for geometrically symmetric samples. The alternative method proposed by Chung should be avoided, especially for non anechoic termination, where strong reflected waves have to be expected.

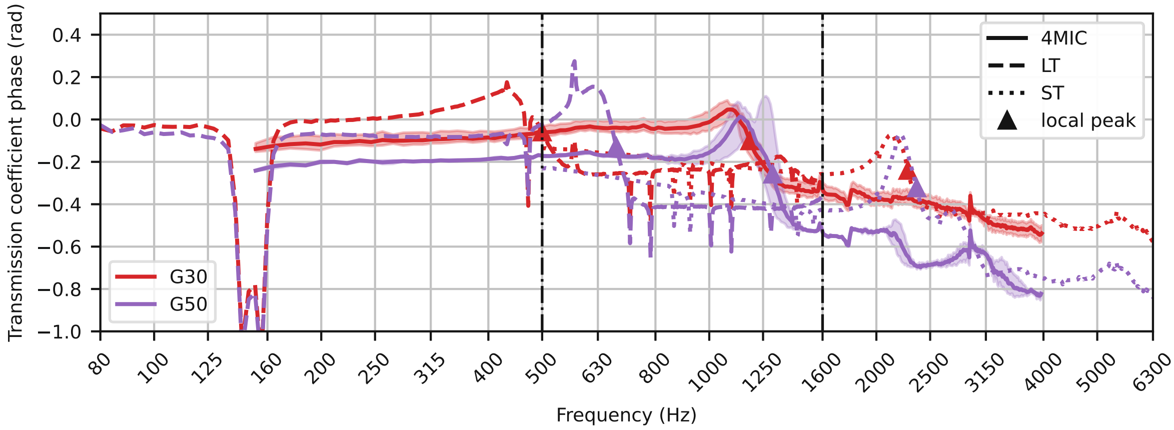

Figure 4.9: Transmission coefficient phases obtained with the four microphone (4MIC) method, compared to small tube (ST) and large tube (LT) baselines for different samples by color. Shaded regions indicate minimum and maximum of the three samples average and triangles mark significant deviations (local peaks).

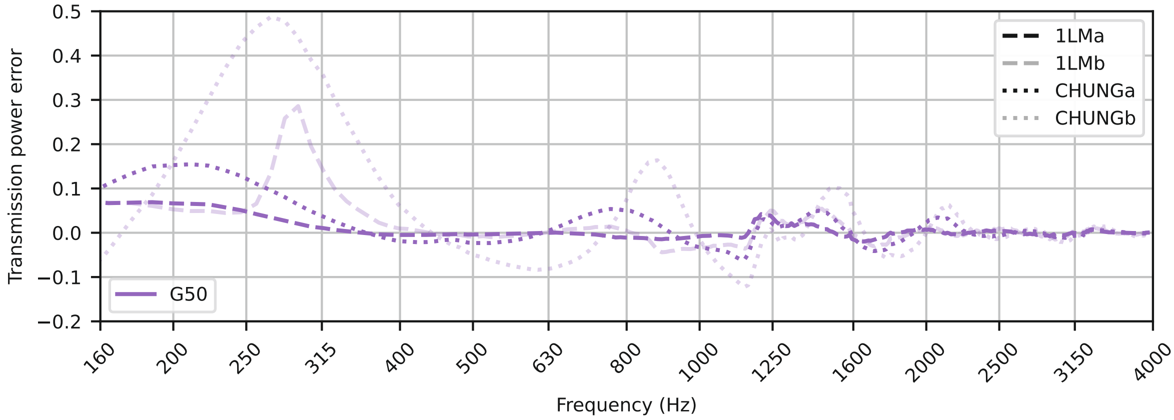

Figure 4.10: Transmission errors obtained with the one-load method (1LM) and alternative definition (CHUNG) in relation to the two-load method (2LM) for G50. Line shades indicate the termination type, where anechoic (a) is solid and open (b) translucent.

4.4 Multiple microphone extension

The main focus of this thesis is the incorporation of additional microphones towards the conventional methods. To evaluate the performance of the posed MISO algorithms in Section 3.3, their results are compared to the baseline measurements. Known problems from Section 4.3 are

- severe deviations at low frequencies strongly depending on pair selection,
- reduced accuracy at the first eigenfrequency for the reflection coefficients, and
- wide-band peaks indirectly proportional to the tube diameter for the transmission coefficient.

The following multi microphone approaches pose a solution to some of these problems, by utilizing all connected microphones. Furthermore, the resulting quantities are expected to extend to very low frequencies, because of wider microphone spacings inside the array design.

4.4.1 Least squares fit

First, the least squares model for the reflection coefficient introduced in Section 3.3.1 is investigated. Therefore, only one microphone module with $M = 8$ microphones is used and connected to the other tube components as shown in setup ⓡ. Three samples are averaged, and the results are plotted in Fig. 4.11, indicating the minimum and maximum deviations as background surfaces. Again the baseline measurements for the commercial LT and ST are displayed as reference. Due to the additional microphones, some of them are spaced further apart, allowing this method to work up to very low frequencies. The resulting total average errors, computed with Eq. (4.2.2), are listed in Table 4.6. The reflected power errors over frequency are attached in Appendix B.

Because of the wider microphone spacings, this method shows great low frequency extension. However, closely spaced microphones are also considered for low frequencies adding inaccuracies to the system. This is explained in Section 4.3.2 and causes a constant increase in error for lower frequencies. Because data is processed in equally spaced discrete frequency points, but plotted logarithmically, errors at lower frequency seem large, but pose a small contribution to the average power error. By comparison to the average of all microphone pairs, the least squares (LSTSQ) method exhibits strongly improved performance. However, in contrast to the optimal pair, a slight increase in error is observed. Therefore, only two of five samples meet the criterion defined in Eq. (4.2.2), although the behavior in the range of the two microphone method does not really change on visual inspection.

Secondly, the LSTSQ model is used to conduct the transmission measurement. The two microphone modules and the other impedance tube components are arranged in setup $\textcircled{\tau}$. The transmission coefficient is measured for three specimens per material, computed with the LSTSQ algorithm, and averaged. To allow a fair comparison to the baseline, the 2LM is used. The outcome of these experiments is displayed in Fig. 4.11, where the baseline measurements are plotted as reference. Minimum and maximum are indicated as translucent surfaces. The average power errors are computed with Eq. (4.2.4) and listed in Table 4.6. The power transmission errors, plotted over frequency, can be found in Appendix B.

Due to wider microphone spacings in the array configuration this method extends to very low frequencies. However, at low frequencies the same phenomena as for the reflection coefficients are observed. These slight low frequency drifts seems to be caused by narrow microphones contributing to the solution over the full frequency range and therefore intensifying inaccuracies in the system. Note that in comparison to the large spread for individual pairs, seen in Fig. 4.7, the error is greatly reduced. What seems to be a constant offset at low frequency, is more likely the low frequency error. This can be argued by looking at the differences between LSTSQ results and ST baselines in the crossover region and comparing them to the differences between LSTSQ and LT for frequencies below 500 Hz. Additionally, operator and specimen cutting effects between tubes are possible reasons for the visible offsets [17]. The results show the previously discussed peaks, indicated as triangles, which are explained in detail in Section 4.3.4. Other than that, the transmission coefficients show no visual change in the range of the 4MIC method. The average errors are again slightly worse, presumably caused by microphone deviations averaging out over the whole frequency range.

Table 4.6: Averaged reflected and transmitted power errors of least squares (LSTSQ) method by sample.

	B30	B50	G20	G30	G50
$\alpha_{\text{e, LSTSQ}}$	0.0630	0.0439	0.0620	0.0575	0.0492
$\tau_{\text{e, LSTSQ}}$	-	-	-	0.0652	0.0811

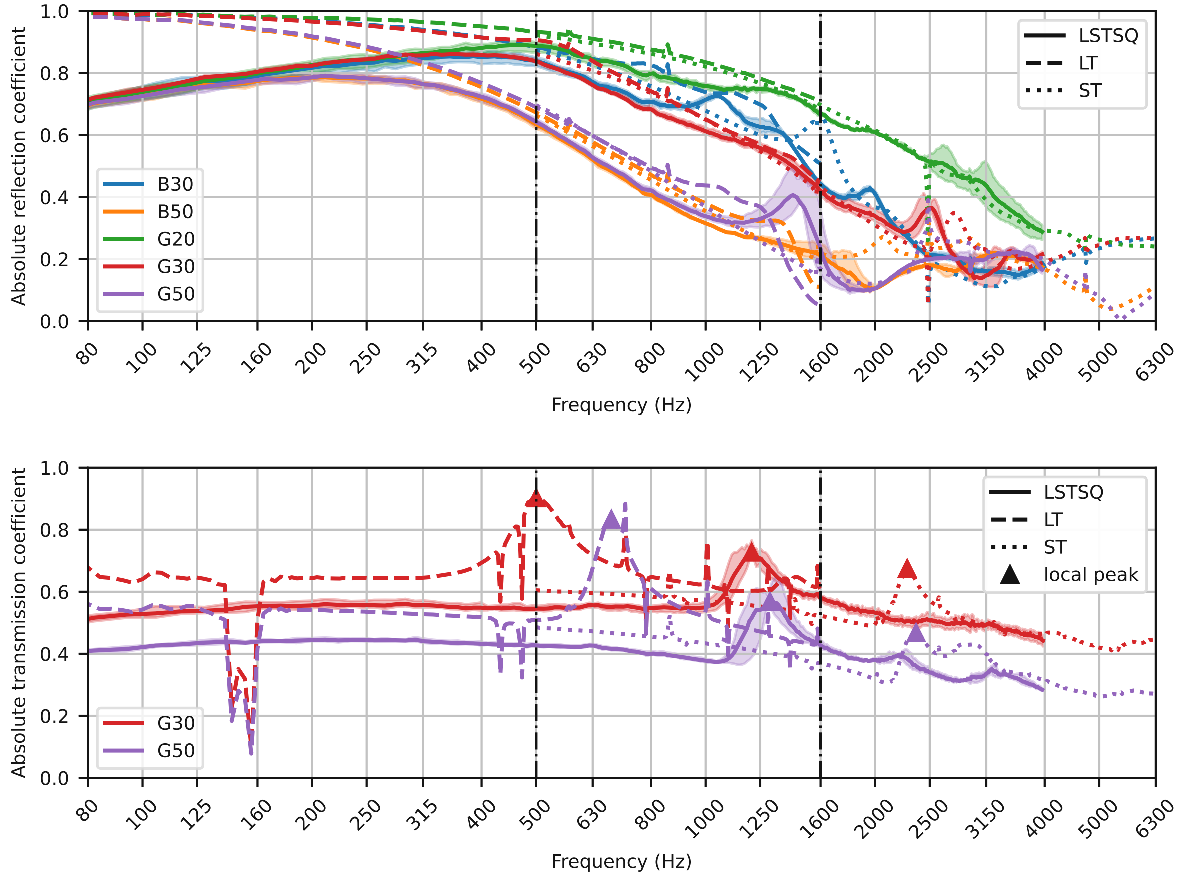

Figure 4.11: Reflection (top) and transmission (bottom) coefficients obtained with the least squares (LSTSQ) method, compared to small tube (ST) and large tube (LT) baselines for different samples by color. Shaded regions indicate minimum and maximum of the three samples average and for transmission (bottom) triangles mark significant deviations (local peaks).

4.4.2 Multiple pair measurement

The multiple pair method iterates over unique microphones pairs or quads, applying the 2MIC or 4MIC method. The results are then averaged, considering their valid frequency ranges. The exact definitions are described in Section 3.3.2. This method closely reassembles the standardized measurements, basically incorporating multiple individual measurements into the same tube.

To measure the reflection coefficient using the MPAIR method, the impedance tube is arranged in setup (r). To evaluate the measurement compared to the baseline, the results are plotted alongside the respective ST and LT baselines of each material, summarized in Fig. 4.12. Again a min-max surface indicates the variations over the three measured samples. To quantify the performance the average power error defined in Eq. (4.2.2) is used. These quantities are listed by material in Table 4.7 and more detailed insights on the errors frequency behavior are attached in Appendix B.

The reflection coefficients, obtained by the MPAIR algorithm, stand out for their low frequency

Table 4.7: Averaged reflected and transmitted power errors of multiple pair (MPAIR) method by sample

	B30	B50	G20	G30	G50
$\alpha_{\text{e, MPAIR}}$	0.0582	0.0393	0.0567	0.0521	0.0443
$\tau_{\text{e, MPAIR}}$	-	-	-	0.0641	0.0801

extension. In contrast to the LSTSQ results, the reflection coefficients are not constantly increasing in error at lower frequencies, but show better approximation to the baseline until ≈ 160 Hz. Below that the error jumps back down to LSTSQ level. The position of this step matches the lower frequency limit of microphone pairs spaced $s_{\text{min}} = 35\,\text{mm}$. Due to the equal spacing, most of the microphone pairs are at this distance, with only a few pairs spaced $2s_{\text{min}}$ or even fewer spaced $3s_{\text{min}}$. Therefore, most of the averages occur above 160 Hz and the average results from the $2s_{\text{min}}$ spaced microphones are shifted in frequency, posing a non continuous transfer. Ideas to handle this issue are discussed in Section 5.2. The middle and high frequencies are unremarkable, closely reassembling the results of other methods. Comparing the average power errors, again only two of five materials pass the bar. However, there is a slight improvement over the LSTSQ method.

To conduct the MPAIR measurement for the transmission coefficient both microphone modules are used and configured in setup τ. Unique microphone quads can exhibit different spacings for up- and downstream tube. Keep in mind that the frequency limits are always defined by the stricter of the two pairs. Derivations and more details on this behavior can be found in Section 3.3.2. Measurements for each sample and termination type were conducted and the results are once more compared to the established baseline in Fig. 4.12. To enable the comparability by scalar values the averaged transmitted power errors are listed in Table 4.7 for both materials.

Similar to the reflection coefficients the most interesting part of the results plotted in Fig. 4.12 can be observed at the lower frequency range. Results at high frequencies once again show no visible change. Due to equal microphone spacing and selected pairs being active for only selected frequency ranges, limited by rectangular windows, one can observe a small step at ≈ 160 Hz. This was previously discussed for the MPAIR reflection coefficients, but for transmission the step appears to be less significant. This could be due to the total of 16 microphones used, resulting in more unique combinations and therefore more averages. Looking at the average power errors, while not exactly significant, there is once more a slight improvement in contrast to the LSTSQ algorithm. Note that both algorithms do not perform up to the specified error criterion.

4.5 Comparison of methods

In previous sections the different methods are compared, evaluated and quantified in respect to the baseline measurements. In this section the measurement results of posed methods are compared to each other visually, by the average power error defined in Section 4.2 and by computational effort. Because displaying all methods for all materials in a single plot is not possible, the comparison graphs are split by material. Examplary, G50 is used for the discussion, but other materials show similar results. Comparison plots of all tested materials can be found in Appendix E.

The different reflection coefficient algorithms are compared in Fig. 4.13 (top) showcasing the discussed trends in the low frequency area and at the node positions at 680 Hz, which are discussed in detail in Section 4.3.2. Except for the jump of the MPAIR algorithm at 160 Hz, both multi microphone algorithms match closely and, except for the discussed deviations, also track well to the baseline. The manufacturer's (BASF) datasheets of the used materials Basotect B [10] and Basotect G+ [11] specify the absorption coefficients over frequency. By rearranging Eq. (2.4.11) the absolute reflection coefficient is expressed as

$$|r| = \sqrt{1 - \alpha}\,. \tag{4.5.1}$$

By transforming the provided absorption data to reflection coefficients, one can additionally compare the results to the manufacturer's data, also plotted in Fig. 4.13, adding to the plausibility of the results. To quantify the accuracy, the averaged reflected power errors of all methods and materials are collected

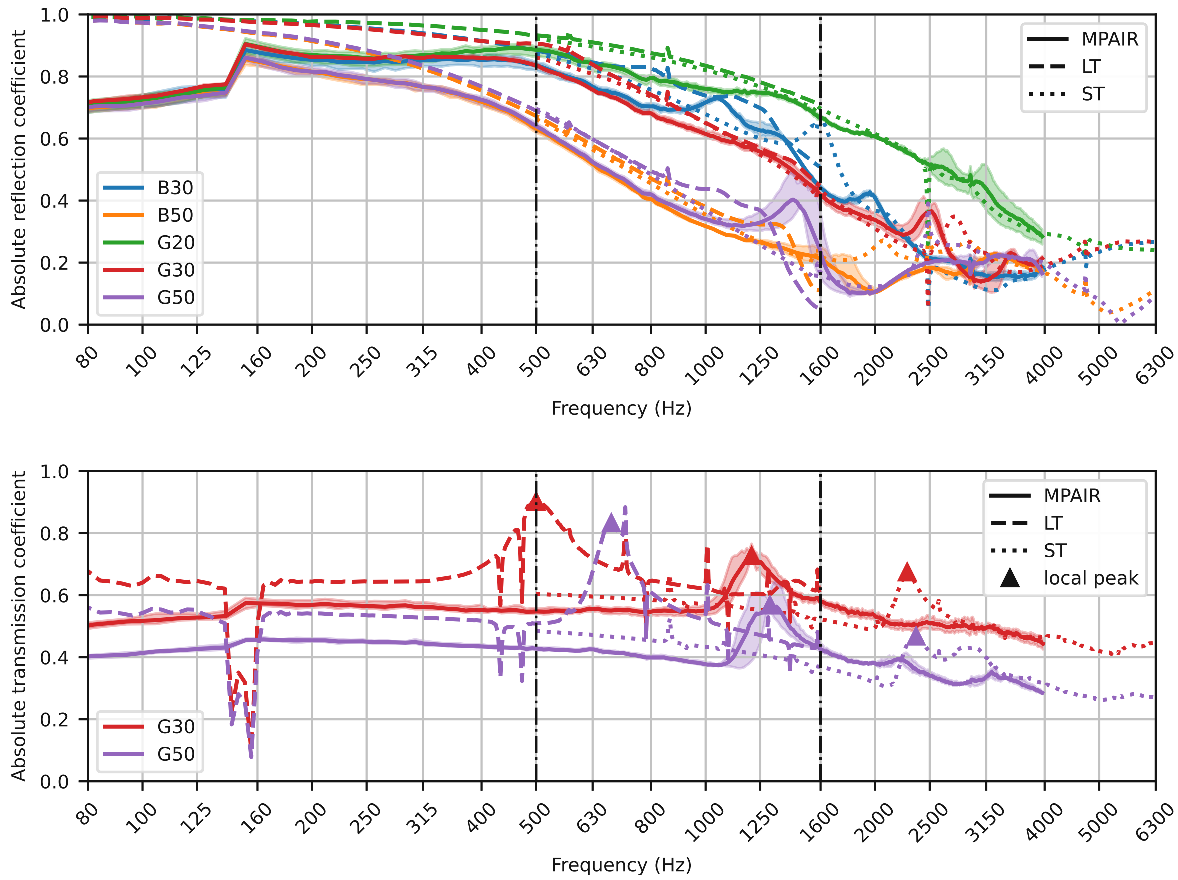

Figure 4.12: Reflection (top) and transmission (bottom) coefficients obtained with the multiple pair (MPAIR) method, compared to small tube (ST) and large tube (LT) baselines for different samples by color. Shaded regions indicate minimum and maximum of the three samples average and for transmission (bottom) triangles mark significant deviations (local peaks).

in Table 4.8. Additionally, the standard deviations of the unique pair investigations are given. Not considering the frequency range, one can see that the closest pair to the specimen, used for the 2MIC method, performed best. For the full frequency range, utilizing all pairs with the 2MIC method shows the largest error for all measured materials. In contrast, the multi microphone techniques managed to greatly reduce the error, with the MPAIR method performing slightly better than the LSTSQ fit. To compare the computational effort, the time durations needed to compute the reflection coefficients are compared, omitting file load, file write, and the averaging process. This benchmark was performed on Windows 11 64bit running on an Intel i5-1135G7 processor. The process is set to high priority and only runs on a single core to ensure consistent results. The computation times are compared in Fig. 4.14 (top). Besides the 2MIC method outperforming both solves, one can see that the LSTSQ algorithm is about five times slower than the MPAIR method. This strongly depends on the amount of microphones used. For $M = 8$ microphones 24 unique combinations are possible, resulting in 24 analytical solves for the MPAIR method, prior to the windowed average, while the LSTSQ just solves one over-determined system for each discrete frequency.

To evaluate the different transmission coefficient methods, their results for G50 are visually compared in Fig. 4.13 (bottom), where the local peaks, discussed in Section 4.3.4, are marked with triangles. Once more a close match between both multi microphone methods is observed, while the 4MIC method exhibits a strong drift below 315 Hz. The jump, observed for the reflection coefficient MPAIR methods at 160 Hz, is barely visible for the transmission results. This is due to the larger number of averages

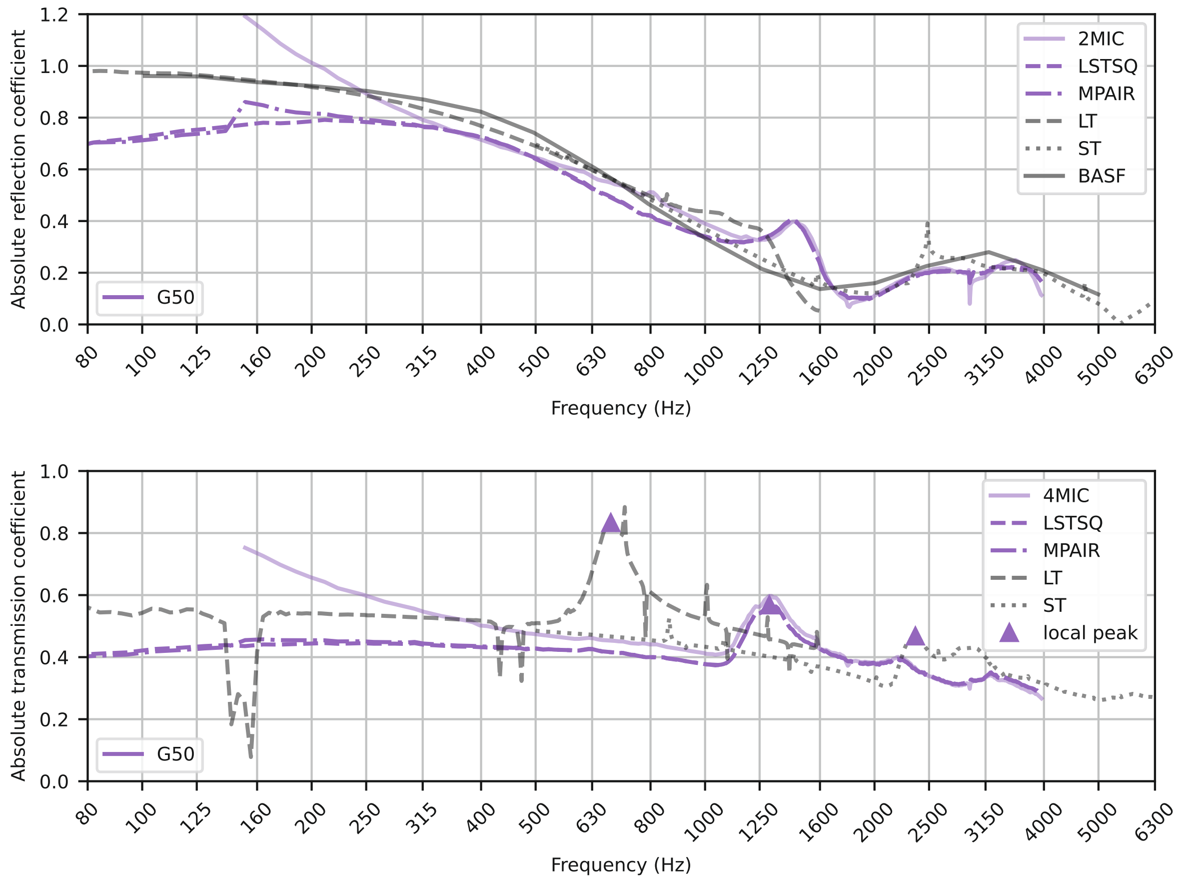

Figure 4.13: Reflection (top) and transmission (bottom) coefficients obtained by different methods and small tube (ST) and large tube (LT) baselines for G50. For transmission (bottom) triangles mark significant deviations (local peaks).

caused by the additional downstream microphones. Because the manufacturer (BASF) does not publish transmission related data, an additional verification of the results is not possible. The results are once more compared by average power error and are gathered in Table 4.8, where the all unique quads tests additionally denotes the standard deviation. Again the 4MIC method outperformed all other methods, but is only valid for higher frequencies. Comparing the multi microphone techniques to the results for all quads, one can see largely reduced errors. The MPAIR method performs slightly better than the LSTSQ method. The computation times, for the same hardware setup as for the reflection coefficient benchmark, are plotted in Fig. 4.14 (bottom). Although the microphone count only doubled, there are 576 unique quads, significantly slowing down the MPAIR method. For the LSTSQ fit the size of the system matrices increased, but due to efficient solvers the computation times only tripled. Therefore we can conclude, that for large microphone counts the LSTSQ fit solves more efficiently, while for low microphone counts the MPAIR method wins by only requiring a few analytical solves. By parallelization of the MPAIR method, i.e. computing the single pair or quad solves on separate cores, the processing could be sped up significantly.

Table 4.8: All averaged reflected and transmitted power errors, for all pairs with standard deviations by sample.

	B30	B50	G20	G30	G50
$\alpha_{\text{e, 2MIC}}$	0.0449	0.0257	0.0365	0.0417	0.0307
$\alpha_{\text{e, all-2MIC}}$	0.0989 ± 0.0418	0.0626 ± 0.0299	0.1035 ± 0.0456	0.0865 ± 0.0380	0.0730 ± 0.0333
$\alpha_{\text{e, LSTSQ}}$	0.0630	0.0439	0.0620	0.0575	0.0492
$\alpha_{\text{e, MPAIR}}$	0.0582	0.0393	0.0567	0.0521	0.0443
$\tau_{\text{e, 4MIC}}$	-	-	-	0.0630	0.0776
$\tau_{\text{e, all-4MIC}}$	-	-	-	0.1193 ± 0.0294	0.0978 ± 0.0205
$\tau_{\text{e, LSTSQ}}$	-	-	-	0.0652	0.0811
$\tau_{\text{e, MPAIR}}$	-	-	-	0.0641	0.0801

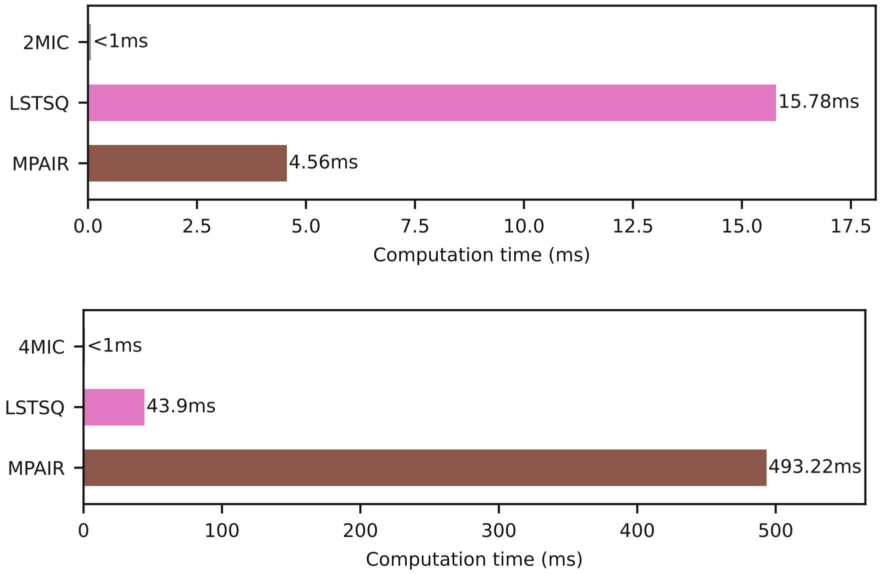

Figure 4.14: Single core computation time on i5-1135G7 for the different reflection- (top) and transmission coefficient methods (bottom).

Chapter 5

Summary and conclusion

5.1 Summary

The experiments in this thesis investigated the effects of consumer grade hardware on impedance tube measurements. Additional to the conventional methods, two newly introduced multi microphone algorithms were tested. To evaluate the performance fifteen samples of five different materials were measured and compared to baseline measurements conducted at Technical University of Graz, utilizing Brüel & Kjær's Type 4206 impedance and transmission loss measurement tubes. To summarize, for the reflection coefficient

- the two microphone (2MIC) method,
- all-pairs with the 2MIC method,
- the least squares (LSTSQ) fit and
- the multiple pair (MPAIR) measurement

were tested. The results of each method were visually compared to the baseline and quantified by the average power error introduced as a measure of deviation in Section 4.2. Additionally, the results were compared to reference absorption values specified by the manufacturer.

Similar measurements were conducted for the transmission coefficient, establishing a reference point for future use of the newly introduced methods. In summary, the investigated methods are

- the four microphone one-load method (1LM) for both terminations,
- Chung's four microphone method for both terminations,
- the four microphone (4MIC) two-load method (2LM),
- all-quads with the four microphone (4MIC) 2LM,
- the least squares (LSTSQ) fit with following 2LM and
- the multiple pair (MPAIR) measurement with following 2LM.

The differences between the various four microphone options were discussed in Section 4.3.5. Therefore, only the latter four tests are of interest for the discussion. Because the manufacture does not specify transmission data, the additional comparisons had to be omitted.

5.2 Conclusion

Despite the discussed errors, rooting at the most basic parts of the measurement setup, microphones and specimens, the posed multi microphone approaches showed promise across all the different experiments. When considering the average error of the different pair and quad measurements, one can see a significant improvement for LSTSQ and MPAIR processing. Due to some pairs and quads adding a substantial amount of error, the proposed algorithms could not outperform the optimally selected pair or quad. However, by considering the broad spread of data fed into the algorithms, multi microphone approaches proved to handle these errors quite well, considering the average pairs, or even the all-pair's performance.

One might think the multiple pair errors should be similar to the all-pair's and all-quad's errors, however, the difference depends strongly on the point where the error is computed. By averaging the results with the multiple pair method, prior to computing the error, the contributions of the different microphone pairs or quads are averaged out, resulting in good error rejection in comparison to the all-pair's and all-quad's errors, where the absolute errors are computed for each unique pair or quad individually.

By comparing the two different multi microphone approaches, it is clear that the MPAIR method performed better for all tested materials. The reason is the selection of valid frequency bands prior to averaging. While the LSTSQ algorithm just averages all inputs at once, the MPAIR method only uses microphone pairs or quads at their optimal frequency range. However, this also showed some drawbacks at the crossover frequencies, where considerable jumps of the resulting quantity were observed. By utilizing smoother window functions, in place of the used rectangular windows, the crossover could be smoothed out. An alternative approach would be the use of unequal microphone spacing to spread the valid frequency ranges across the spectrum and reduce the effect of uneven distribution at specific frequency bins. Judging by performance, for high microphone counts the LSTSQ average wins, by computing the wave decomposition with one least squares solve, while the MPAIR method iterates over all unique pairs, decomposing the waves for each individually. Utilizing parallelization, the MPAIR method could be sped up considerably. For low microphone counts the MPAIR algorithm is faster, because it does not require to solve an over-determined system.

One of the main findings of this thesis is once more the importance of accurate and precisely calibrated measurement equipment. Especially for critical points i.e. low frequencies, or nodal points of eigenfrequencies, where very small pressure deviations have to be processed. For this cases small errors can cause large deviations in measurement results. Some ideas on how to improve these errors are presented in Section 5.3.

5.3 Outlook

Because some baseline results experienced bad overlap in the crossover region, additional measurements are recommended for these samples. Special care should be taken to ensure consistent cutting and sample mounting by the same operator, to reduce external impact factors on the measurement results.

One of the main problem was the error at low differences. To tackle this problem, the custom built microphones should be reevaluated and their low signal and noise characteristics should be tested. Note that a main factor for small differences is their signal to noise ratio. To eliminate calibration errors, different types of calibrations and references should be tested. A full anechoic termination would additionally allow in place calibration by eliminating the reflected wave and therefore longitudinal modes of the tube. Other than that, the multiple microphone approaches show great potential to allow super wide frequency range measurements in a single tube diameter efficiently averaging errors of individual microphone pairings. This shifts the bottleneck to the excitation, where different concepts of low frequency excitation in small tubes could be explored.

The hardware used for the experiments looks promising, but several improvements are recommended for future experiments. First of all, the terminations for the 2LM need to be improved. The used anechoic termination, an absorptive foam plug, only showed good absorption factors for frequencies above 500 Hz. For blocked/open termination an open end was used allowing surrounding noise to enter the tube. By small modifications the reflective piston from setup (r) could also be used as termination for setup (τ).

Finally it poses a great extension to this thesis to apply the introduced algorithms to different existing impedance tube setups and to compare the results with the prior measured baselines. The data used in this thesis is limited, not just because of the bad low differences performance, but also due to the low sample size of five foam samples used. Another set of experiments will most certainly substantiate the findings of this thesis.

Bibliography

[1] M. C. M. Wright. "A short history of bad acoustics". In: *The Journal of the Acoustical Society of America* 120.4 (Oct. 2006), pp. 1807–1815. DOI: 10.1121/1.2336746.

[2] David Cahan. "From dust figures to the kinetic theory of gases". In: *Annals of Science* 47.2 (Mar. 1990), pp. 151–172. DOI: 10.1080/00033799000200181.

[3] Michael Möser. *Technische Akustik*. Berlin, Heidelberg: Springer Berlin Heidelberg, 2015. ISBN: 978-3-662-47704-5. DOI: 10.1007/978-3-662-47704-5.

[4] ISO. *Acoustics — Determination of sound absorption coefficient and impedance in impedance tubes Part 2: Transfer-function method*. Genève, 2023. DOI: 10.31030/3501828.

[5] ASTM. *Standard Test Method for Normal Incidence Determination of Porous Material Acoustical Properties Based on the Transfer Matrix Method*. Oct. 18, 2019. DOI: 10.1520/E2611-19.

[6] Reinhard Lerch, Gerhard Sessler, and Dietrich Wolf. *Technische Akustik*. Berlin, Heidelberg: Springer Berlin Heidelberg, 2009. ISBN: 978-3-540-49833-9. DOI: 10.1007/978-3-540-49833-9.

[7] Alan V. Oppenheim and Ronald W. Schafer. *Discrete-Time Signal Processing*. 3rd ed. Edinburgh Gate, Harlow: Pearson Education Limited, 2014. ISBN: 1-292-02572-7.

[8] ASTM. *Standard Test Method for Impedance and Absorption of Acoustical Materials Using a Tube, Two Microphones and a Digital Frequency Analysis System*. Nov. 13, 2019. DOI: 10.1520/E1050-19.

[9] J. Y. Chung and D. A. Blaser. "Transfer function method of measuring in-duct acoustic properties. I. Theory". In: *The Journal of the Acoustical Society of America* 68.3 (Sept. 1, 1980), pp. 907–913. DOI: 10.1121/1.384778.

[10] BASF. *Basotect B*. Datasheet. BASF SE, Apr. 2015.

[11] BASF. *Basotect G+*. Datasheet. BASF SE, June 2016.

[12] Sung Soo Jung et al. "Measurement of Sound Transmission Loss by Using Impedance Tubes". In: *Journal of the Korean Physical Society* 53.2 (Aug. 14, 2008), pp. 596–600. DOI: 10.3938/jkps.53.596.

[13] David Havelock, Sonoko Kuwano, and Michael Vorländer, eds. *Handbook of signal processing in acoustics*. New York, NY: Springer, 2008. ISBN: 978-0-387-77698-9.

[14] George S. K. Wong. "Characteristic impedance of humid air". In: *The Journal of the Acoustical Society of America* 80.4 (Oct. 1, 1986), pp. 1203–1204. DOI: 10.1121/1.394468.

[15] George S. K. Wong and Tony F. W. Embleton. "Variation of the speed of sound in air with humidity and temperature". In: *The Journal of the Acoustical Society of America* 77.5 (May 1, 1985), pp. 1710–1712. DOI: 10.1121/1.391918.

[16] Bosch Sensortec GmbH. *Humidity sensor BME280*. 2023. URL: https://www.bosch-sensortec.com/products/environmental-sensors/humidity-sensors-bme280/ (visited on 01/12/2024).

[17] Merten Stender et al. "Explainable machine learning determines effects on the sound absorption coefficient measured in the impedance tube". In: *The Journal of the Acoustical Society of America* 149.3 (Mar. 1, 2021), pp. 1932–1945. DOI: 10.1121/10.0003755.

[18] A. F. Seybert and Benjamin Soenarko. "Error analysis of spectral estimates with application to the measurement of acoustic parameters using random sound fields in ducts". In: *The Journal of the Acoustical Society of America* 69.4 (Apr. 1981), pp. 1190–1199. DOI: 10.1121/1.385700.

[19] J. N Reddy. *Theory and analysis of elastic plates and shells*. 2. ed. Boca Raton: CRC, 2007. ISBN: 0-8493-8415-X. DOI: 10.1201/9780849384165.

[20] Kin Ming Ho et al. "Measurements of sound transmission through panels of locally resonant materials between impedance tubes". In: *Applied Acoustics* 66.7 (July 2005), pp. 751–765. DOI: 10.1016/j.apacoust.2004.11.005.

Appendix A

Baseline measurements

A.1 Reflection coefficients

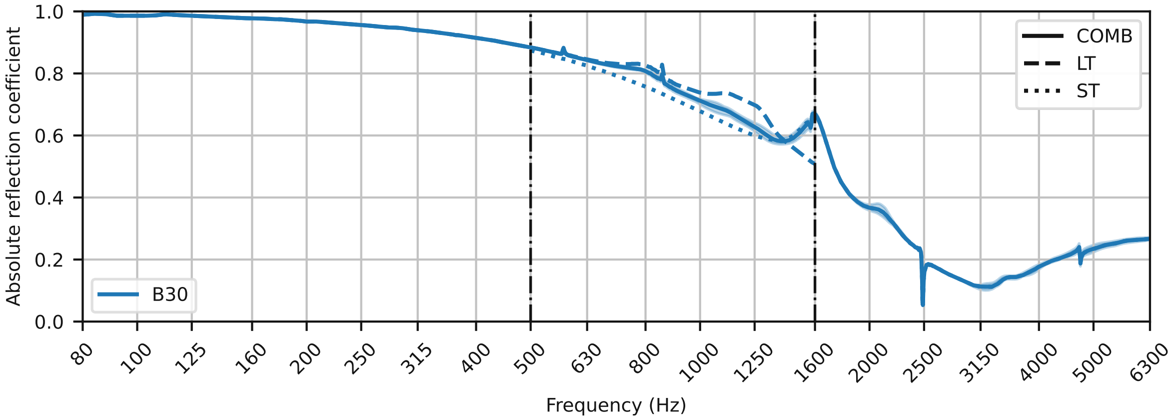

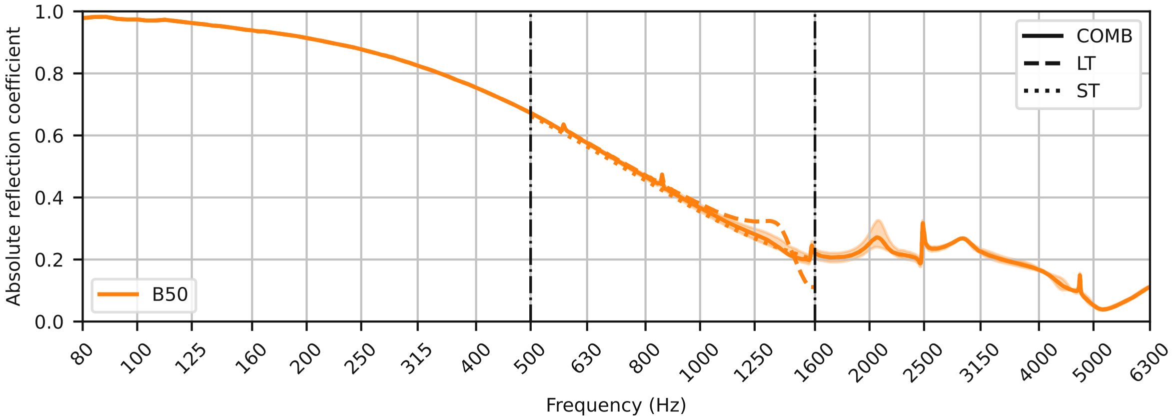

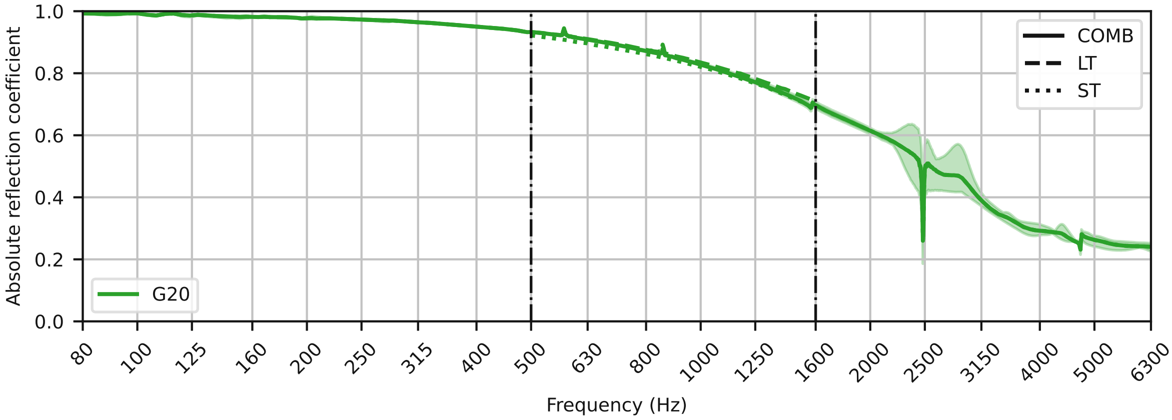

Absolute reflection coefficient
Frequency (Hz)
COMB
LT
ST
G20

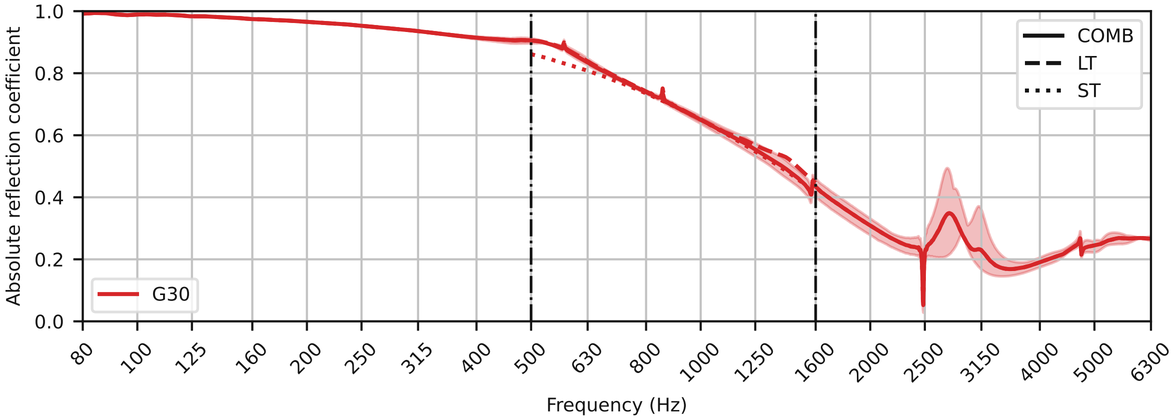

Absolute reflection coefficient
Frequency (Hz)
COMB
LT
ST
G30

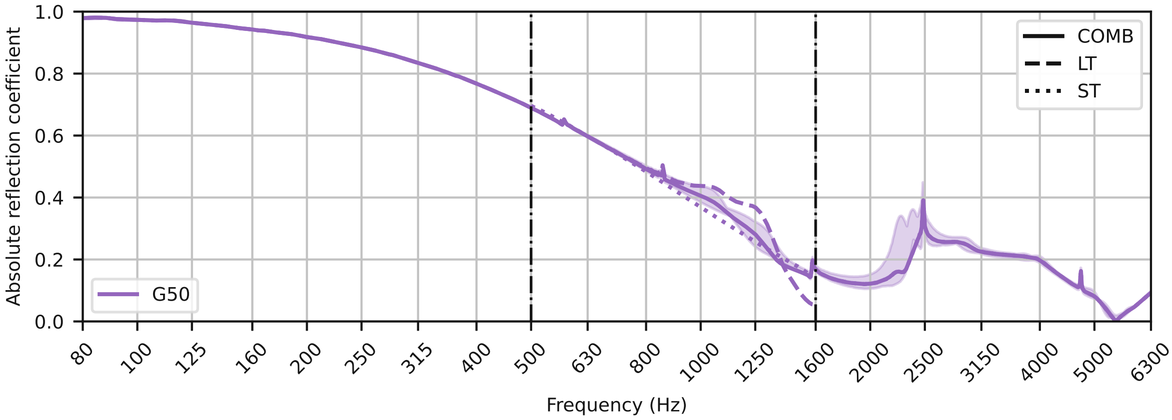

Absolute reflection coefficient
Frequency (Hz)
COMB
LT
ST
G50

A.2 Transmission coefficients

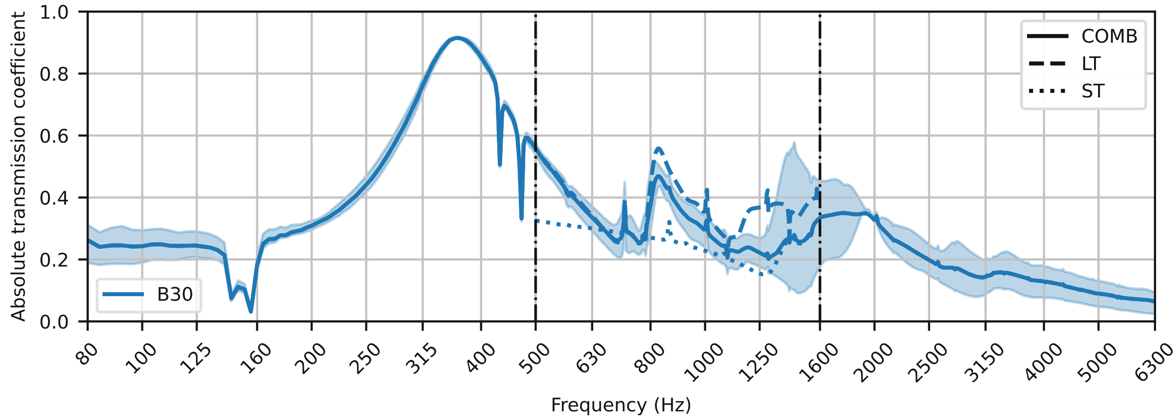

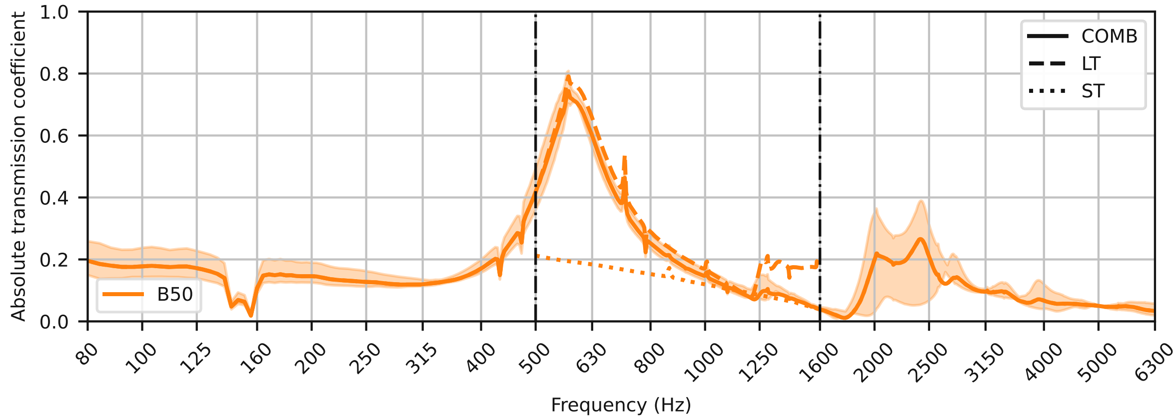

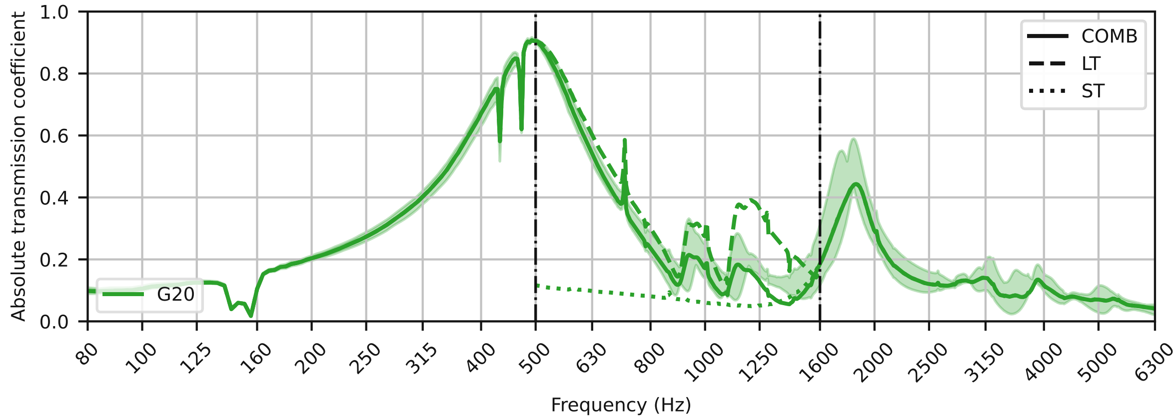

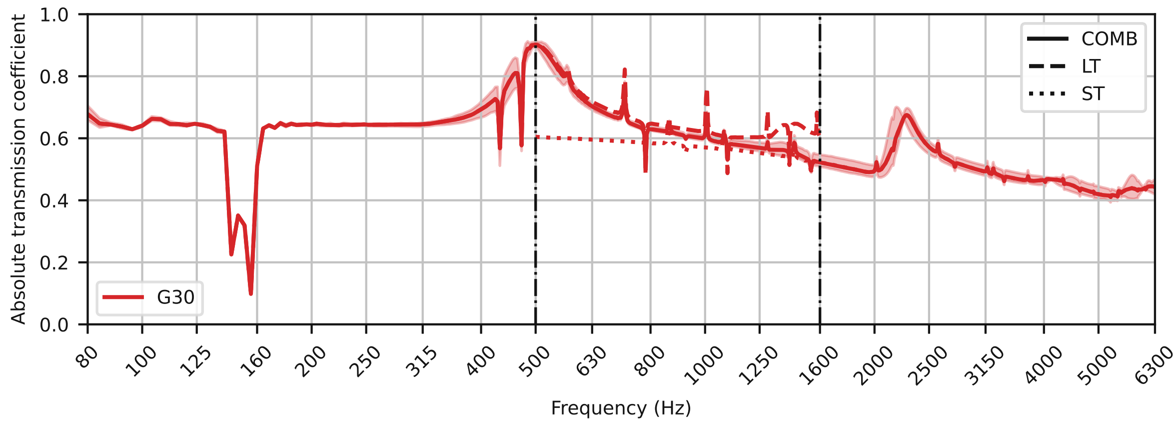
Absolute transmission coefficient
Frequency (Hz)
COMB
LT
ST
G30

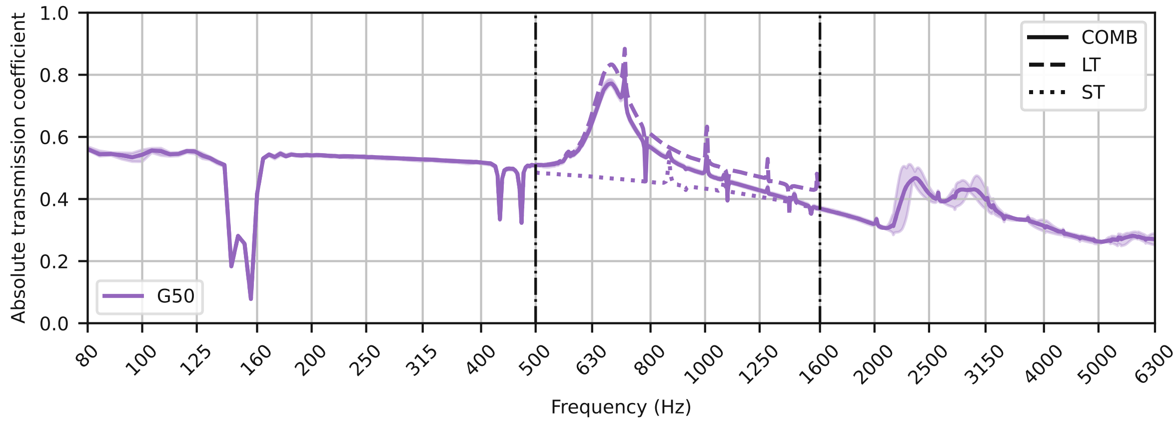
Absolute transmission coefficient
Frequency (Hz)
COMB
LT
ST
G50

Appendix B

Power errors by method

B.1 Reflection power errors

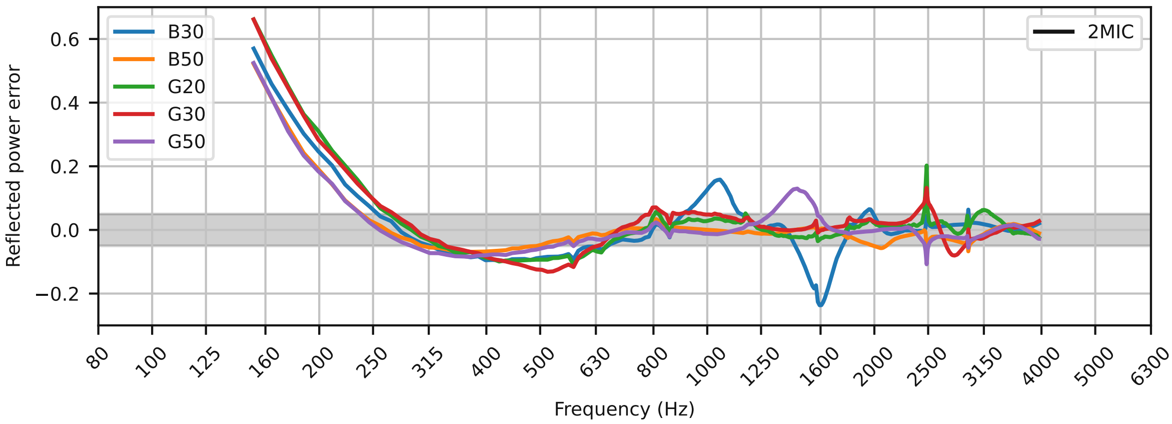

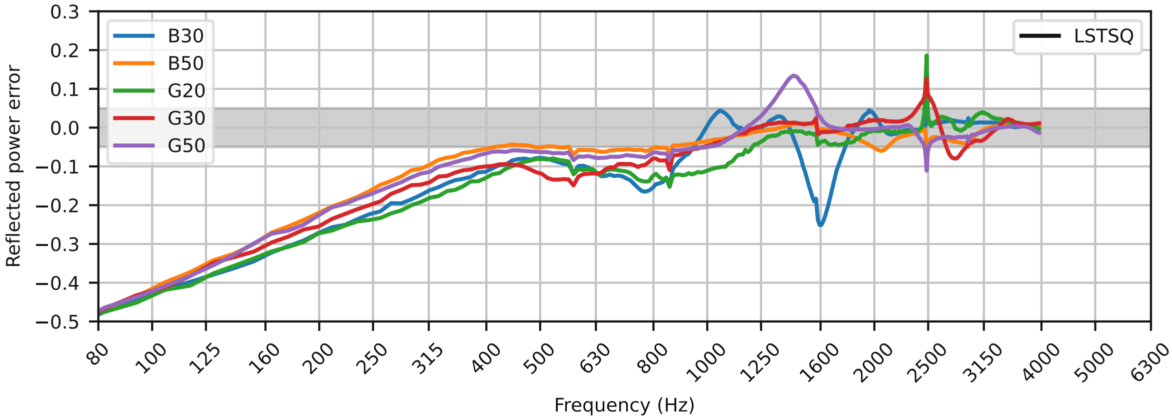

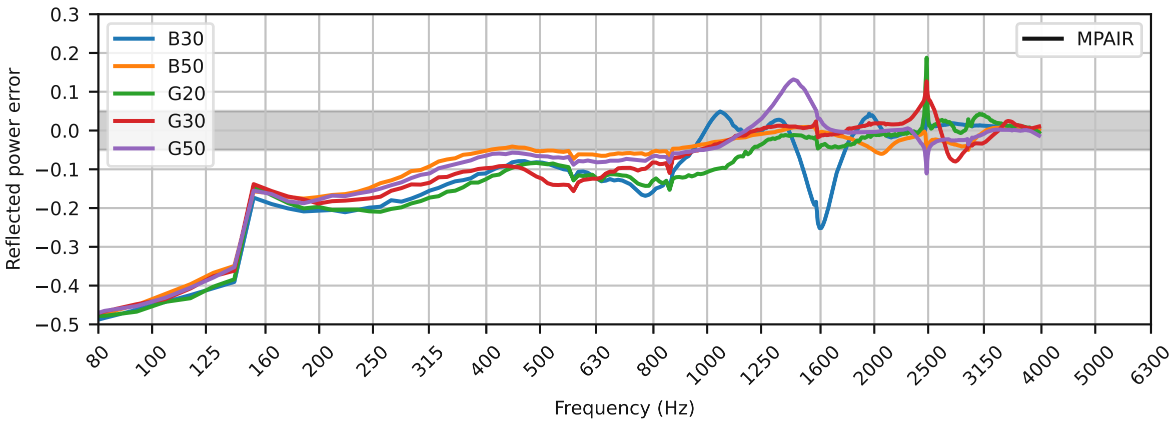

B.2 Transmission power errors

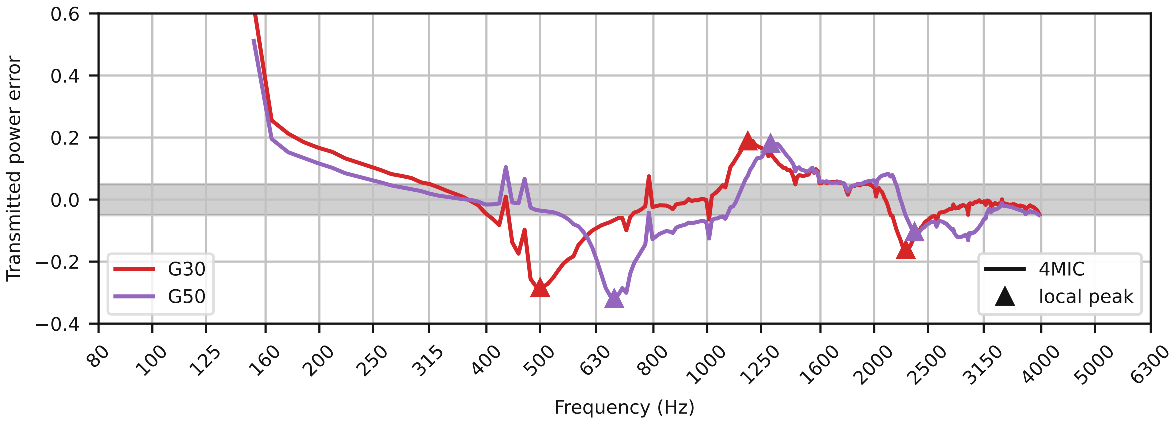

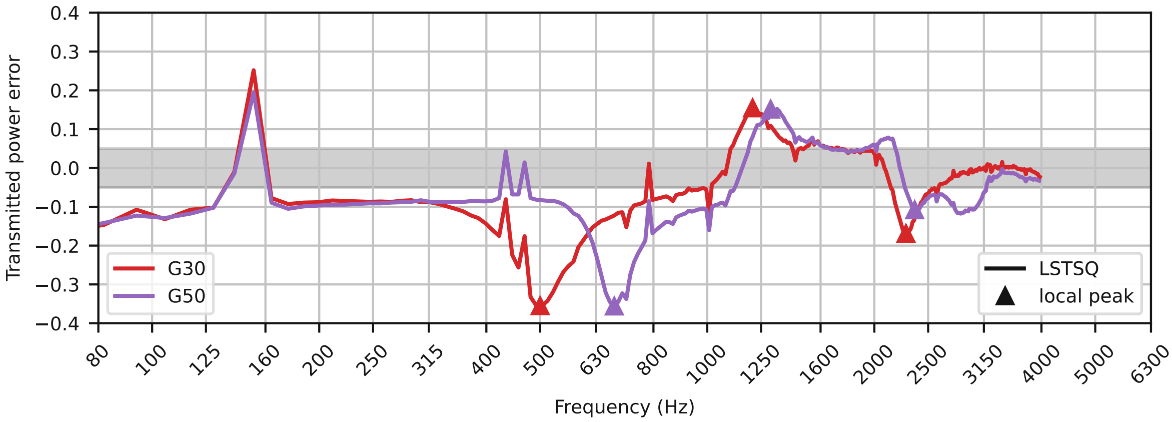

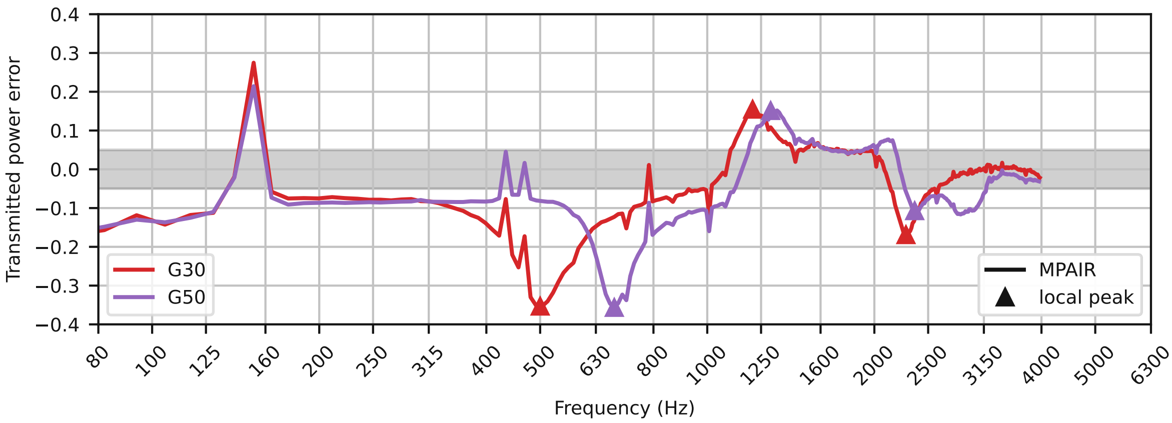
Transmitted power error
Frequency (Hz)
0.4
0.3
0.2
0.1
0.0
−0.1
−0.2
−0.3
−0.4
80
100
125
160
200
250
315
400
500
630
800
1000
1250
1600
2000
2500
3150
4000
5000
6300
G30
G50
MPAIR
local peak

Appendix C

Deviations for different pair/quad selection

C.1 Reflection power errors

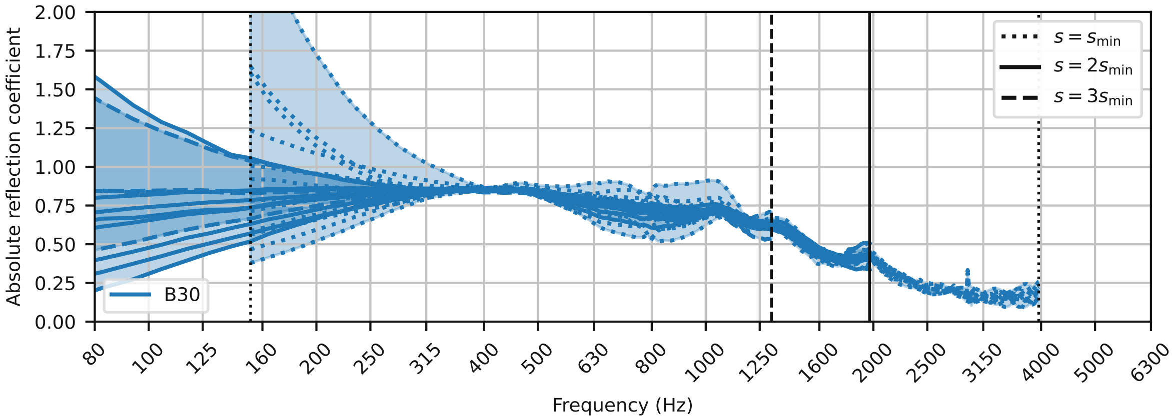

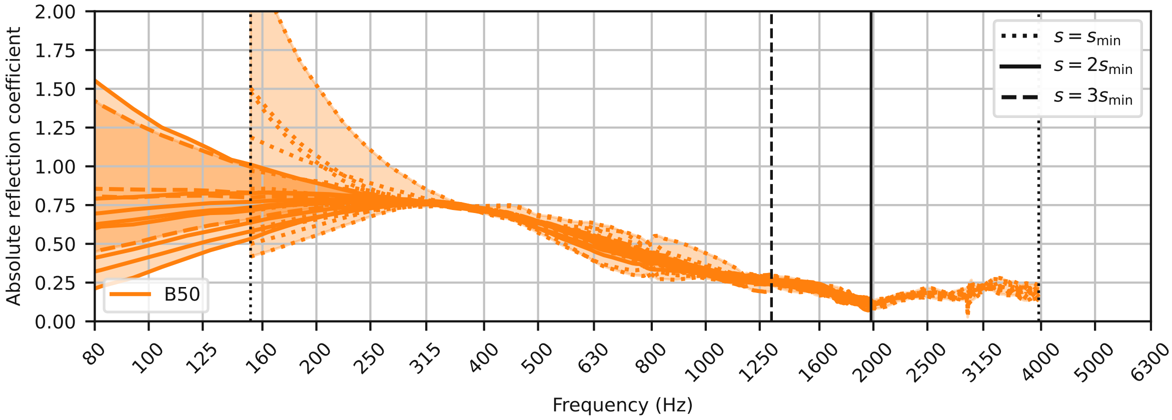

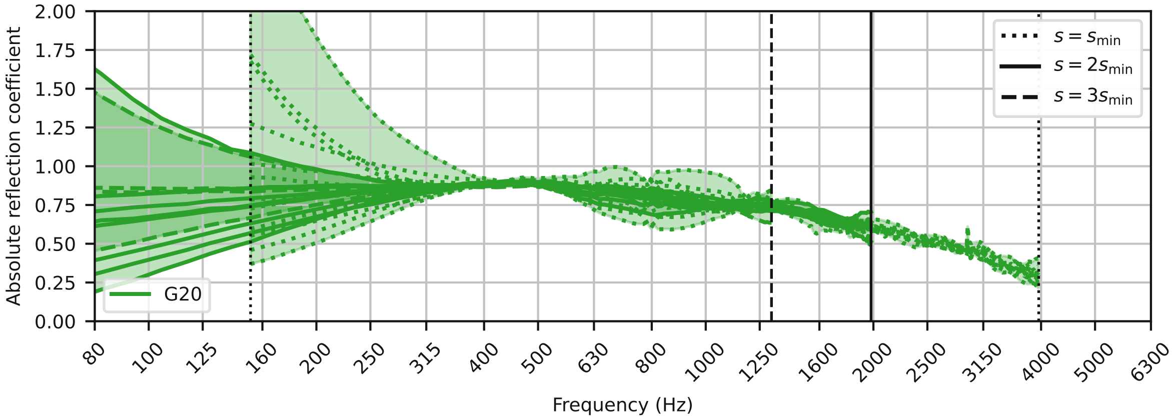
Absolute reflection coefficient
Frequency (Hz)
G20
$s = s_{\min}$
$s = 2s_{\min}$
$s = 3s_{\min}$

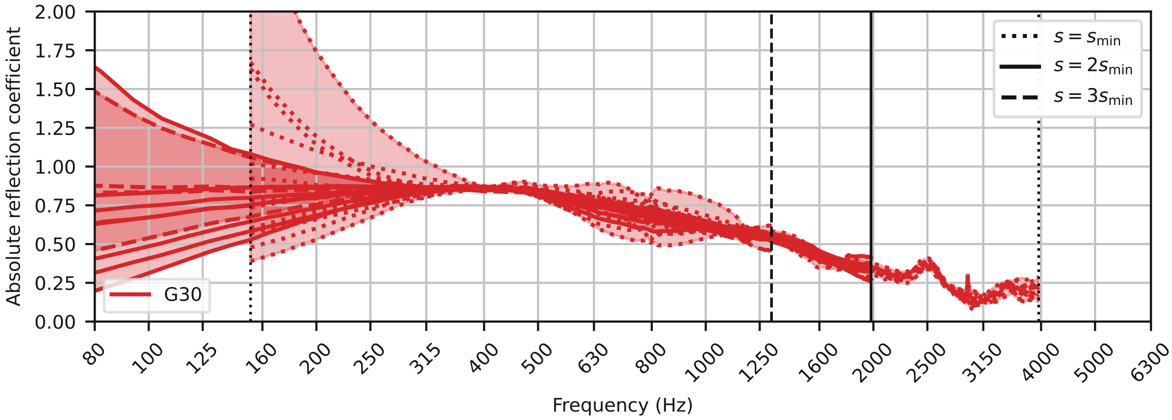
Absolute reflection coefficient
Frequency (Hz)
G30
$s = s_{\min}$
$s = 2s_{\min}$
$s = 3s_{\min}$

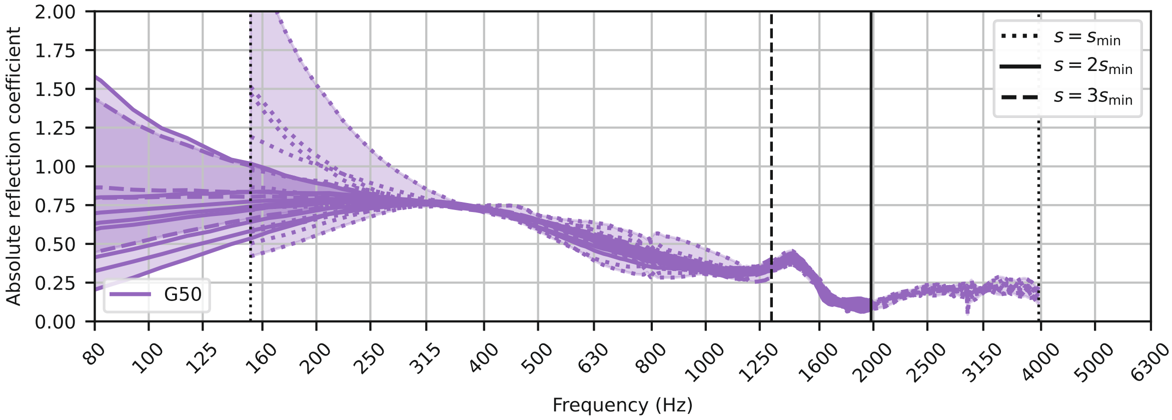
Absolute reflection coefficient
Frequency (Hz)
G50
$s = s_{\min}$
$s = 2s_{\min}$
$s = 3s_{\min}$

C.2 Transmission power errors

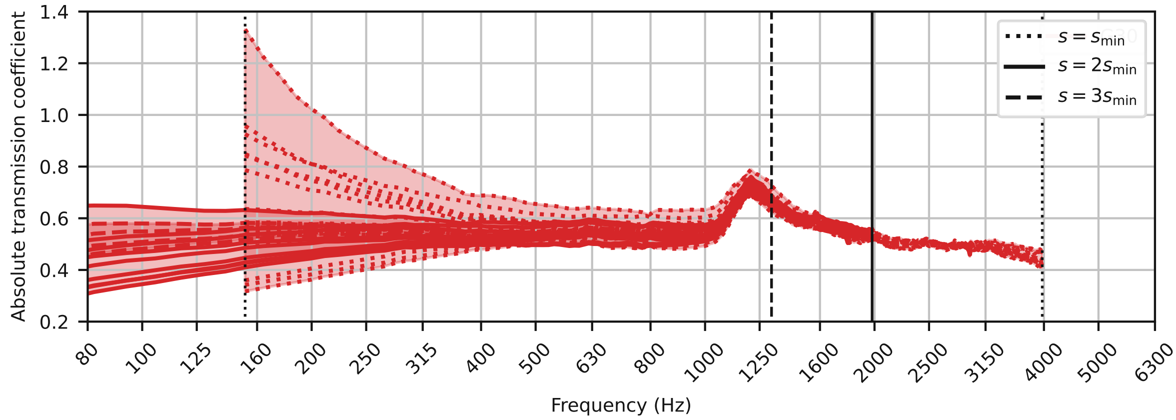

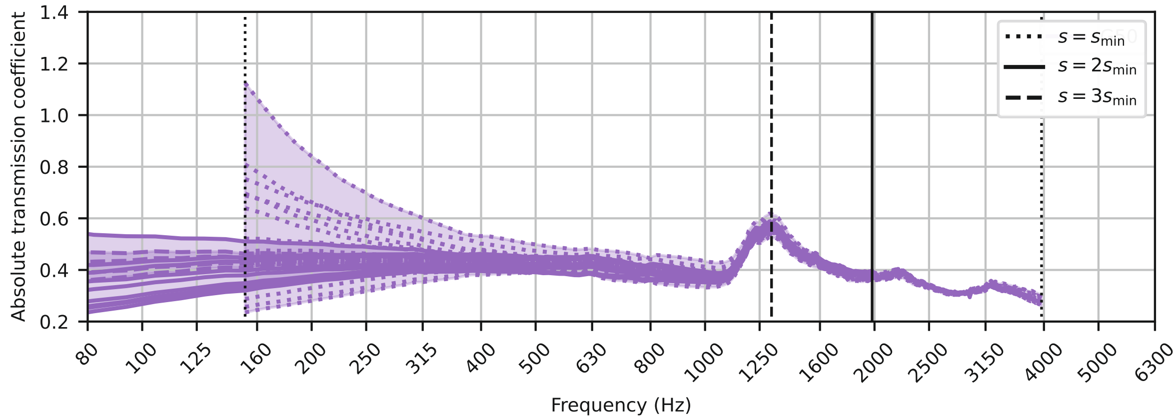

Appendix D

Influence of reflected waves

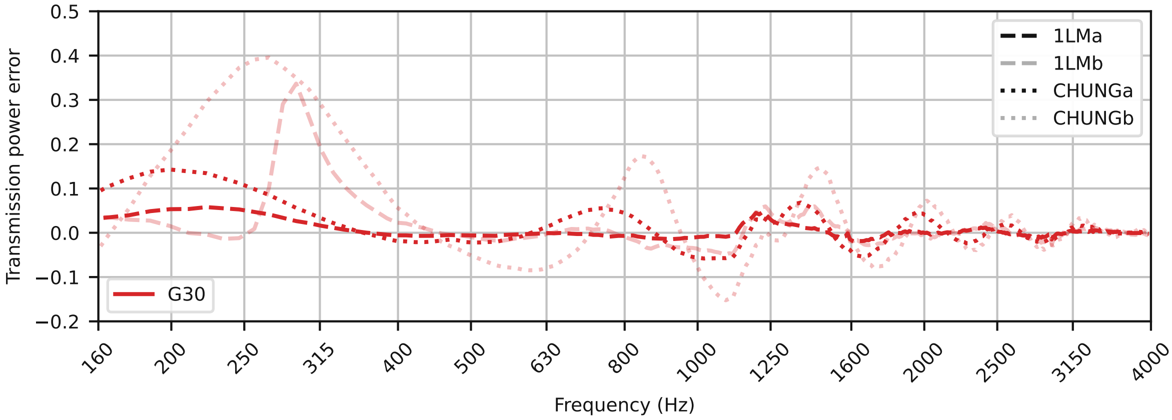

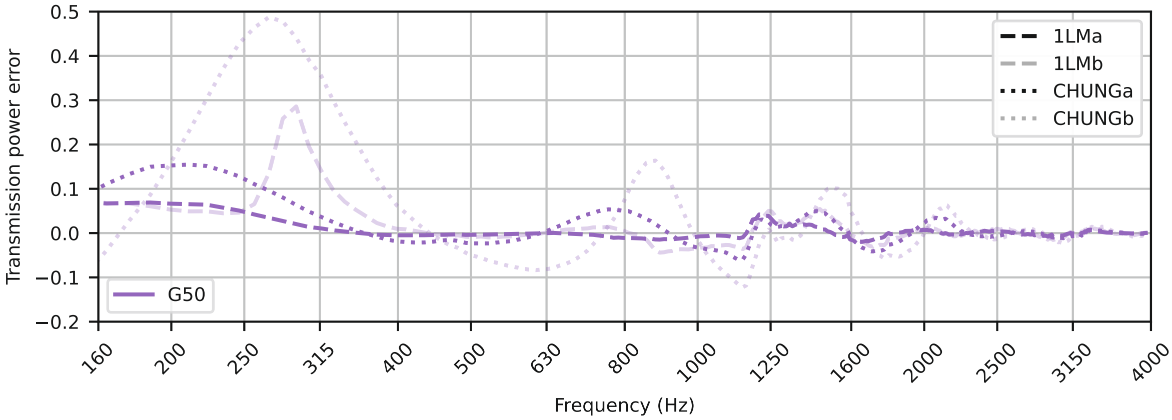

Appendix E

Comparison of methods

E.1 Reflection coefficients

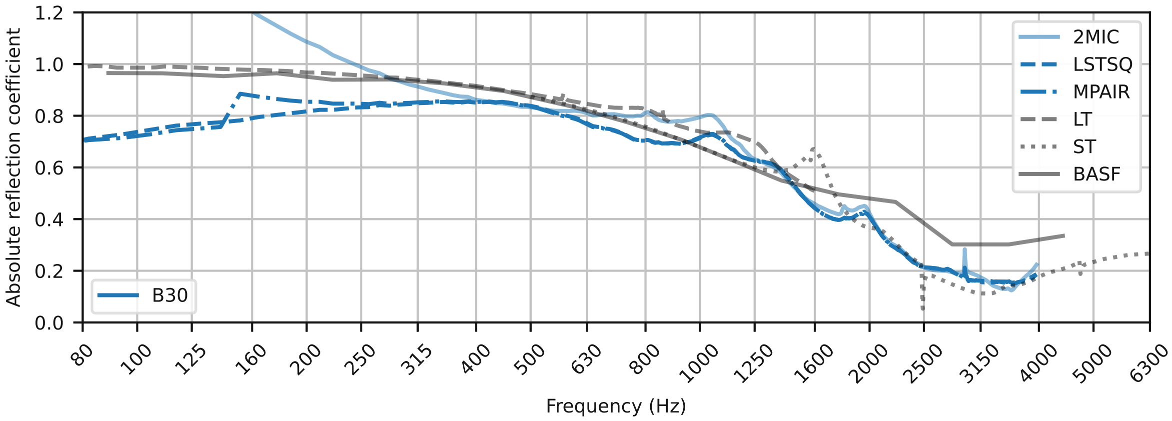

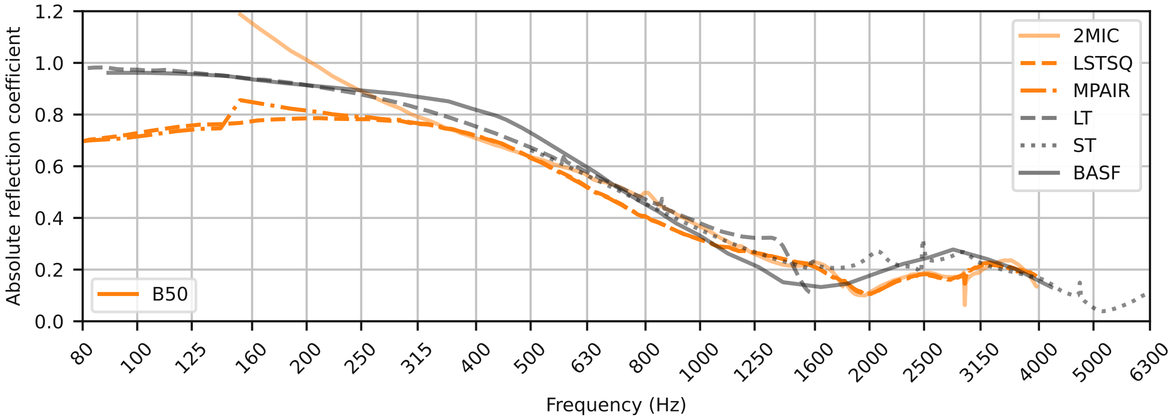

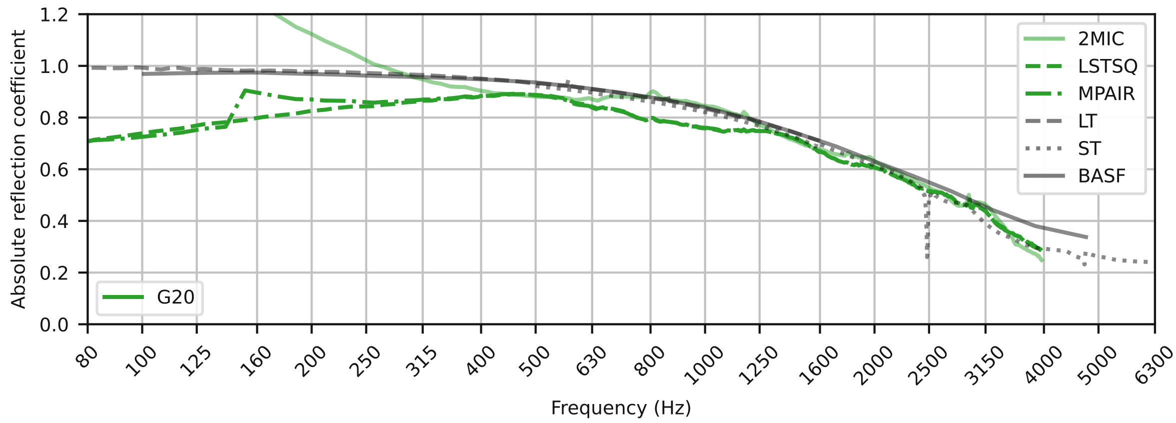
Absolute reflection coefficient
Frequency (Hz)
2MIC
LSTSQ
MPAIR
LT
ST
BASF
G20

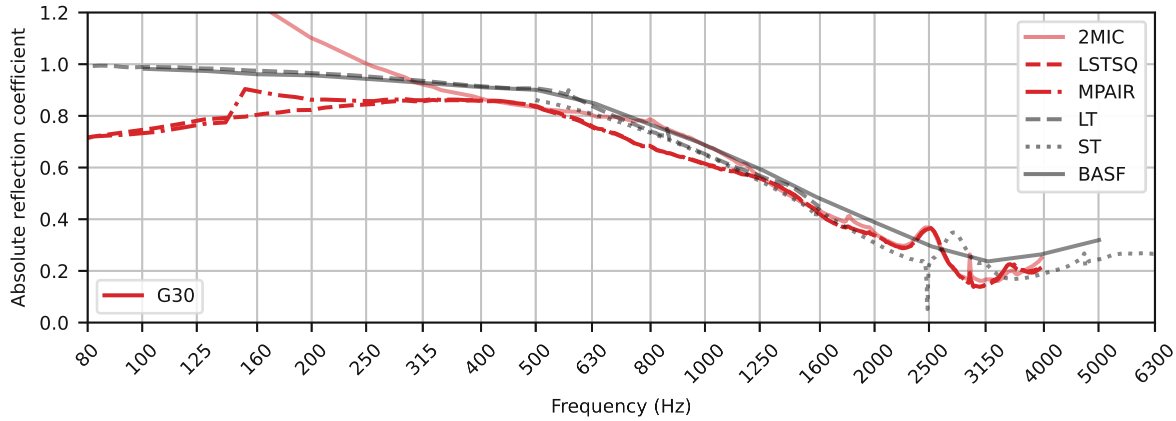
Absolute reflection coefficient
Frequency (Hz)
2MIC
LSTSQ
MPAIR
LT
ST
BASF
G30

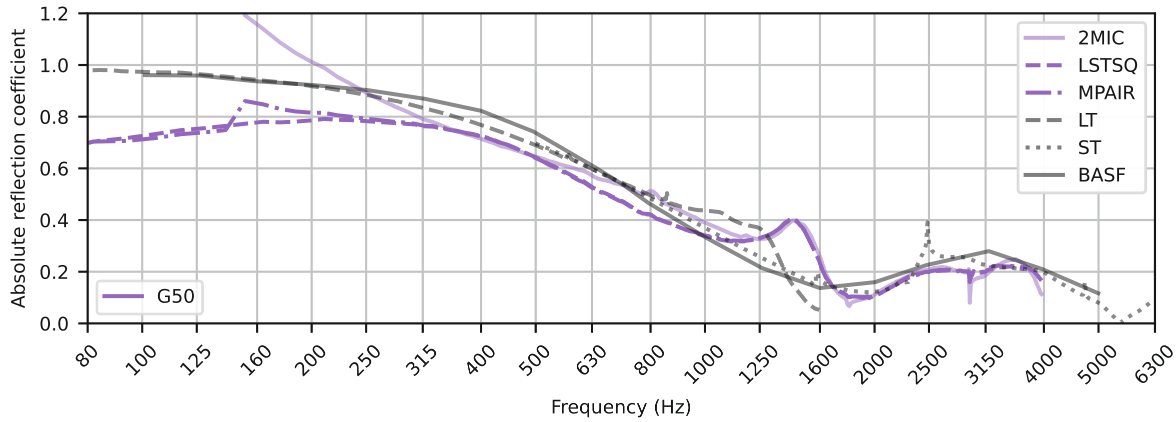
Absolute reflection coefficient
Frequency (Hz)
2MIC
LSTSQ
MPAIR
LT
ST
BASF
G50

E.2 Transmission coefficients